

PERFORMANCE PREDICTION OF
NOZZLELESS SOLID PROPELLANT ROCKET MOTORS

A THESIS SUBMITTED TO
THE GRADUATE SCHOOL OF NATURAL AND APPLIED SCIENCES
OF
MIDDLE EAST TECHNICAL UNIVERSITY

BY

ALİ CAN ÖZER

IN PARTIAL FULFILLMENT OF THE REQUIREMENTS
FOR
THE DEGREE OF MASTER OF SCIENCE
IN
AEROSPACE ENGINEERING

SEPTEMBER, 2015

Approval of the thesis:

**PERFORMANCE PREDICTION OF
NOZZLELESS SOLID PROPELLANT ROCKET MOTORS**

submitted by **ALİ CAN ÖZER** in partial fulfillment of the requirements for the degree of **Master of Science in Aerospace Engineering Department, Middle East Technical University** by,

Prof. Dr. Gülbin Dural Ünver
Dean, Graduate School of **Natural and Applied Sciences**

Prof. Dr. Ozan Tekinalp
Head of Department, **Aerospace Engineering**

Prof. Dr. Yusuf Özyörük
Supervisor, **Aerospace Engineering Dept., METU**

Examining Committee Members

Assoc. Prof. Dr. Sinan Eyi
Aerospace Engineering Dept., METU

Prof. Dr. Yusuf Özyörük
Aerospace Engineering Dept., METU

Assoc. Prof. Dr. Oğuz Uzol
Aerospace Engineering Dept., METU

Assist. Prof. Dr. Sıtkı Uslu
Mechanical Engineering Dept., TOBB UET

Assist. Prof. Dr. Mustafa Kaya
Dept. of Flight Training., UTAA

Date:

11.09.15

I hereby declare that all information in this document has been obtained and presented in accordance with academic rules and ethical conduct. I also declare that, as required by these rules and conduct, I have fully cited and referenced all material and results that are not original to this work.

Name, Last name: Ali Can ÖZER

Signature :

ABSTRACT

PERFORMANCE PREDICTION OF NOZZLELESS SOLID PROPELLANT ROCKET MOTORS

Özer, Ali Can

M.S., Department of Aerospace Engineering

Supervisor: Prof. Dr. Yusuf Özyörük

September 2015, 90 pages

Integral rocket ramjet (IRR) type propulsion systems have many advantages over conventional solid rocket motors when used in tactical missile systems. Nozzleless boosters are one of the applicable concept choices for the system [1].

During the design and development phase of solid propellant rocket motors, simulation and prediction of behavior of a given motor by numerical tools is important in terms of decreasing the development duration and costs.

The present approach includes performance prediction of nozzleless solid propellant rocket motors. In order to predict performance and numerically simulate the flow field inside the motor, first internal ballistics of the motor is examined theoretically. Then, quasi one dimensional internal ballistics model is constructed and solved numerically

through inside the motor. In order to predict burning rate, an erosive burning relation has been implemented into the numerical scheme.

To verify the flow solver, results against the Sod shock tube problem is obtained. Grid resolution and time step size sensitivity study is made. The results of numerical internal ballistics simulations are compared with the experimental nozzleless motor firing results found in literature are simulated and compared. Simulations are conducted for both quasi steady and unsteady approach, and outcomes of two approaches are compared as well. Proposed numerical scheme is promising for predicting thrust and pressure histories of nozzleless solid propellant rocket motors. Also from the design point of view, parametric studies are conducted. Effect of grain geometry and propellant burning rate are studied.

Key-words: Nozzleless Solid Propellant Rocket Motor, Internal Ballistics, Quasi One Dimensional Flow

ÖZ

LÜLESİZ KATI YAKITLI ROKET MOTORLARINDA PERFORMANS KESTİRİMİ

Özer, Ali Can

Yüksek Lisans, Havacılık ve Uzay Mühendisliği

Tez Yöneticisi: Prof. Dr. Yusuf Özyörük

Eylül 2015, 90 sayfa

Bütünleşik roket ramjet teknolojisi, taktik füze sistemleri için, geleneksel katı yakıtlı roket motorlarına nazaran oldukça getiri vaad etmektedir. İlk itici olarak lülesiz katı yakıtlı roket motorlarının kullanılması bu sistem için oluşturulan kavram seçeneklerinden biridir [1].

Katı yakıtlı roket motoru tasarım ve geliştirme aşamasında, motor davranış karakteristiklerinin sayısal yöntemlerle benzetimi ve kestirimi geliştirme süresi ve maliyeti açısından önemlidir.

Bu çalışma lülesiz katı yakıtlı roket motoru performans kestirimini içermektedir. Performans kestirimi ve motor içerisindeki akışı benzetebilmek için, motor iç balistiği teorik olarak incelenmiştir. Sonrasında, numerik analizler için kısmi bir boyutlu iç

balistik modeli oluşturulmuştur. Yanma hızı kestirimi için, erozyonlu yanma bağıntıları sayısal şema içerisinde gömülmüştür.

Akış çözücüsünün doğrulanması adına, Sod şok tüpü problem sonuçları elde edilmiştir. Çözüm ağı çözünürlüğünün ve zaman adımı boyutlarının sonuçlara olaran etkileri incelenmiştir. Numerik benzetimlerden elde edilen sonuçlar, literatürde verilmiş olan, lülesiz motor ateşlemesi ile elde edilen deneysel veriler ile karşılaştırılmıştır. Benzetimler, kısmi durağan ve durağan olmayan yaklaşımlarla yapılmış ve iki yaklaşımın sonuçları da karşılaştırılmıştır. Önerilen sayısal şemanın lülesiz katı yakıtlı roket motorlarında, itki ve basınç profillerinin kestirimi açısından gelecek vaad ettiği değerlendirilmektedir. Ayrıca tasarım açısından parametrik çalışmalar yürütülmüştür. Yakıt çekirdeği geometrisinin ve yanma hızı bağıntısının etkileri çalışılmıştır.

Anahtar Kelimeler: Lülesiz Katı Yakıtlı Roket Motoru, İç Balistik, Kısmi Bir Boyutlu Akış

ACKNOWLEDGEMENTS

I would like to express my deepest thanks and gratitude to Prof. Dr. Yusuf ÖZYÖRÜK for his supervision and constant guidance through this study.

I would like to give my special appreciations to the Chief of the Propulsion Systems Division in TÜBİTAK-SAGE, Dr. Bülent SÜMER, for sharing his experience and for his great suggestions throughout this study.

I would like to express my sincere gratitude to my colleagues at TÜBİTAK SAGE, especially Bora YAZICI, Sertaç CURDANELİ and Çetin Ozan ALANYALIOĞLU for their crucial advises and invaluable efforts during the preparation of this thesis.

I would like to thank to my friend Ilgaz Doğa OKCU for his inestimable friendship and patience.

Special thanks go to my mother Gülseren ÖZER, my father Baki ÖZER and my entire family for always being there for me and giving me the motivation.

I am forever grateful for my darling's patience, unfailing support and encouragement during this difficult period.

Lastly, this thesis is dedicated to my family. It would be impossible without their patience and understanding.

TABLE OF CONTENTS

ABSTRACT.....	v
ÖZ.....	vii
ACKNOWLEDGEMENTS.....	ix
TABLE OF CONTENTS.....	x
LIST OF TABLES.....	xii
LIST OF FIGURES.....	xiii
LIST OF SYMBOLS.....	xvi
CHAPTERS	
1. INTRODUCTION.....	1
1.1. MOTIVATION.....	1
1.1.1. Ejectable Nozzle.....	4
1.1.2. Nozzleless Solid Propellant Rocket Motor.....	5
1.2. LITERATURE SURVEY.....	6
1.3. SCOPE OF THE THESIS.....	12
1.4. CONTENT OF THE THESIS.....	12
2. NOZZLELESS SOLID PROPELLANT ROCKET MOTORS.....	15
2.1. FUNDAMENTALS OF NOZZLELESS SPRM.....	15
2.1.1. Main Parts of Nozzleless SPRM.....	15
2.1.2. Internal Ballistics of SPRM.....	18
2.2. INTERNAL BALLISTICS PREDICTION AND ANALYSIS.....	24
2.2.1. 0-Dimensional Quasi Steady Flow Field Models.....	24
2.2.2. 1-Dimensional Quasi-steady and Unsteady Analysis.....	25
2.2.3. 2-Dimensional Unsteady Flow Field Models.....	26
3. COMPUTATIONAL METHODOLOGY.....	27

3.1.	GAS DYNAMICS MODEL	27
3.2.	BURNING RATE RELATION	33
3.3.	FLUX SPLITTING SCHEME	35
3.4.	BOUNDARY CONDITIONS	41
3.5.	SOLUTION ALGORITHM	42
3.5.1.	Unsteady Solution	42
3.5.2.	Quasi-Steady Solution.....	43
4.	VALIDATION RESULTS	45
4.1.	SHOCK-TUBE CASE	45
4.2.	NOZZLELESS SPRM EXPERIMENTAL CASE	49
4.3.	GRID RESOLUTION AND TIME STEP SENSITIVITY.....	51
4.4.	QUASI STEADY SOLUTIONS	57
4.5.	UNSTEADY SOLUTIONS	62
4.6.	DETAILED EXAMINATION OF TEST CASE PREDICTIONS	65
5.	PARAMETRIC STUDIES	73
5.1.	RESULTS.....	74
5.1.1.	Motor X.....	74
5.1.2.	Motor Y.....	77
5.1.3.	Motor Z	79
5.1.4.	Performance Comparison.....	81
6.	CONCLUSION AND FUTURE WORK	85
	REFERENCES.....	87

LIST OF TABLES

TABLES

Table 1: Dimensions of test case geometry	49
Table 2: Specification of motor configurations.	73
Table 3: Performance comparison of different configurations	82

LIST OF FIGURES

FIGURES

Figure 1: Theoretical Performance Envelopes for Ramjet and Solid Propellant Rocket [2].	2
Figure 2: Operational Sequence of Integral Rocket Ramjet Concept [1].	3
Figure 3: Ejectable Nozzle Assembly [3].	5
Figure 4: Schematic diagram of a nozzleless SPRM [4].	15
Figure 5: Typical thrust-pressure curves of a nozzleless propellant grain [17].	22
Figure 6: 0-Dimensional Lumped Parameter Analysis.	25
Figure 7: Slices of Grain Port.	28
Figure 8: Control Volume for one-dimensional model.	28
Figure 9: Adjacent Cells and the Interface.	36
Figure 10: Cell numbering and boundary conditions.	41
Figure 11: Initial Conditions for Sod Shock Tube Problem.	46
Figure 12: Density distribution at $t=1.7$.	47
Figure 13: Pressure distribution at $t=1.7$.	47
Figure 14: Velocity distribution at $t=1.7$.	48
Figure 15: Definitions of dimensions of nozzleless SPRM given in [4].	49
Figure 16: Variation of Burn rate with pressure for the propellant given in [4].	51
Figure 17: Pressure-time profiles for different grid lengths with 0.1 s time steps.	52
Figure 18: Thrust-time profiles for different grid lengths with 0.1 s time steps.	53
Figure 19: Pressure-time profiles for different grid lengths with 0.01 s time steps.	53
Figure 20: Thrust-time profiles for different grid lengths with 0.01 s time steps.	54
Figure 21: Pressure-time profiles for different time steps with 0.01 m grid length.	55
Figure 22: Thrust-time profiles for different time steps with 0.01 m grid length.	55

Figure 23: Pressure-time profiles for different time steps with 0.001 m grid length.	56
Figure 24: Thrust-time profiles for different time steps with 0.001 m grid length...	56
Figure 25: Head end pressure-time profiles of motor A.	58
Figure 26: Thrust-time profiles of motor A.	58
Figure 27: Head end pressure-time profiles of motor B.	60
Figure 28: Thust-time profiles of motor B.....	61
Figure 29: Variation of head end pressure for unsteady and quasi steady approach	63
Figure 30: Variation of thrust for unsteady and quasi steady approach	63
Figure 31: Variation of head end pressure for unsteady and quasi steady approach (close up view of Figure 29)	64
Figure 32: Variation of thrust for unsteady and quasi steady approach (close up view of Figure 30)	65
Figure 33: Mach number distribution along the port for 0.01 m grid length.....	66
Figure 34: Mach number distribution along the port for 0.001 m grid length.....	66
Figure 35: Port radius distribution along the grain for 0.01 m grid length.....	67
Figure 36: Port radius variation along the grain for 0.001 m grid length.	68
Figure 37: Variation of burn rate along the grain for 0.01 m grid length.	69
Figure 38: Variation of burn rate along the grain for 0.001 m grid length.	70
Figure 39: Normal (solid lines) and erosive (dashed lines) burn rate along the grain for 0.01 m grid length	70
Figure 40: Normal (solid lines) and erosive (dashed lines) burn rate along the grain for 0.001 m grid length	71
Figure 41: Grain geometry for motor configurations X and Z.	74
Figure 42: Variation of Head end pressure with time of Motor X	75
Figure 43: Variation of Dimensionless Thrust with time of Motor X	75
Figure 44: Variation of Exit Pressure with time of Motor X.....	76
Figure 45: Variation of Area Expansion Ratio of exit cone with time of Motor X..	77

Figure 46: Variation of Head end pressure with time of Motor Y.....	78
Figure 47: Variation of Dimensionless Thrust with time of Motor Y	78
Figure 48: Variation of exit pressure with time of Motor Y	79
Figure 49: Variation of head-end pressure with time of Motor Z.....	80
Figure 50: Variation of Dimensionless Thrust with time of Motor Z.....	81
Figure 51: Variation of Dimensionless Thrust with time of Motor X, Y and Z.	82

LIST OF SYMBOLS

a	Burning rate coefficient
A_b	Burn area
A_e	Motor gas exit area
E	Total energy per unit mass
F	Thrust
\mathbf{F}	Flux vector
G	Mass flux
g	Gravitational acceleration
I_{sp}	Specific Impulse
I_{tot}	Total Impulse
L_x	Axial Length
\dot{m}	Mass flow rate
\dot{m}_{gen}	Generated mass flow rate
\dot{m}'_{gen}	Generated mass flow rate per unit length
n	Burning rate pressure exponent
P	Pressure
P_{ref}	Reference Pressure
\mathbf{Q}	Solution vector
R	Gas constant
r_0	Normal burning rate
r_b	Burning rate

r_e	Erosive burning rate
\mathcal{S}	Source vector
T	Temperature
u	Velocity
V_e	Motor gas exit velocity

Greek Symbols:

α	Erosive burning coefficient
β	Erosive burning coefficient
γ	Ratio of specific heats
η	Ratio of total burning rate to normal burning rate
ρ	Gas density
ρ_p	Propellant density
μ	Gas viscosity

CHAPTER 1

INTRODUCTION

In this chapter, fundamental information related to integral rocket ramjet and nozzleless solid propellant rocket motors is given. Firstly, motivation for this study is explained. Afterwards, literature survey related to this work is presented. Lastly, scope of the thesis, and content of the thesis is introduced.

1.1. MOTIVATION

Historically, air-to-air missiles have been powered by solid propellant rocket motors (SPRM). This type of motors is relatively simple, reliable, and cheap. They have been quite capable of performing up to the required level for the mission. However, relatively low specific impulse of these motors precludes the range and flight speed of the missile. Moreover, most of the missile's flight path occurs after engine die out, thus the missile flies mostly without thrust, which enhances the enemy's ability to evade being hit. Usage of ramjet type propulsion system for missiles, especially for air-to-air missiles, is very promising. Ramjet engines provide more sustainable thrust and higher specific impulse than Solid Propellant Rocket Motors (SPRM). Moreover, it is possible to control the thrust level of a ramjet engine in its operational envelope. Sustainable thrust of a ramjet engine provides the missile excess power during its operational time. This fact increases the effective range of the missile and allows

various maneuvers until burnout of the ramjet propellant. Maintained high speed decreases the time to target intercept and increases the no escape zone¹ of the missile.

As a known fact, ramjet engines are not able to operate at subsonic speeds and their optimum efficiency is achieved at Mach numbers than 2, as is shown in Figure 1. Due to this fact, it is necessary to have a booster engine to accelerate the missile up to operational regime of the ramjet. The concept of integrating solid rocket motor inside the ramjet engine is called integrated rocket-ramjet (IRR) type of propulsion system.

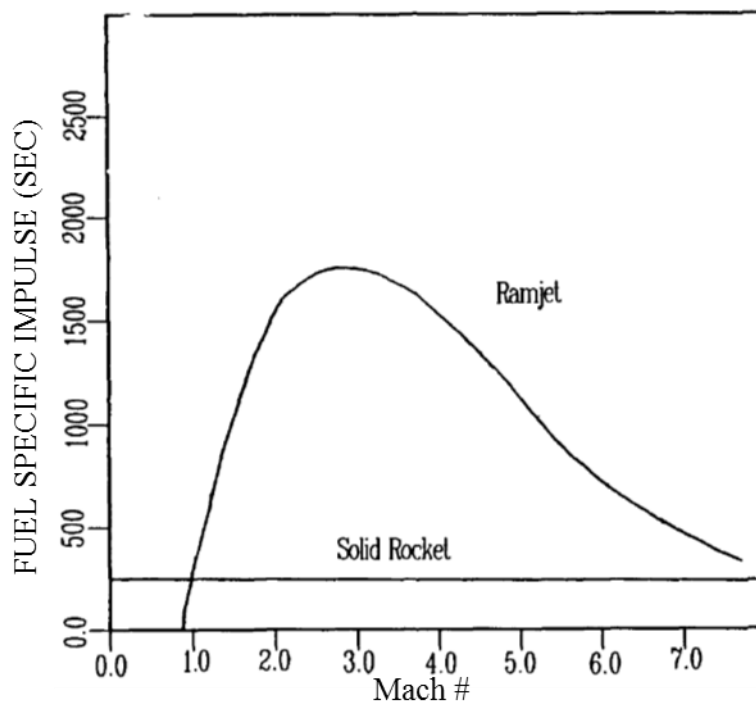


Figure 1: Theoretical Performance Envelopes for Ramjet and Solid Propellant Rocket [2].

¹ No Escape Zone : The zone within which there is a high kill probability against a target even if it has been alerted.

Operational sequence of integrated rocket-ramjet type systems can be summarized as below and in Figure 2.

1. **Launch Phase** : Air intakes and air duct are closed by port cover. Ignition sequence of booster starts.
2. **Boost Phase** : After the propellant ignited, booster motor accelerates the missile up to operational envelope of ramjet engine.
3. **Transition Phase** : After booster burnout, air intakes and port covers are opened, air flow into the ramjet combustor starts.
4. **Sustain Phase** : Ramjet engine provides necessary thrust for the missile to satisfy the requirements of the flight trajectory.

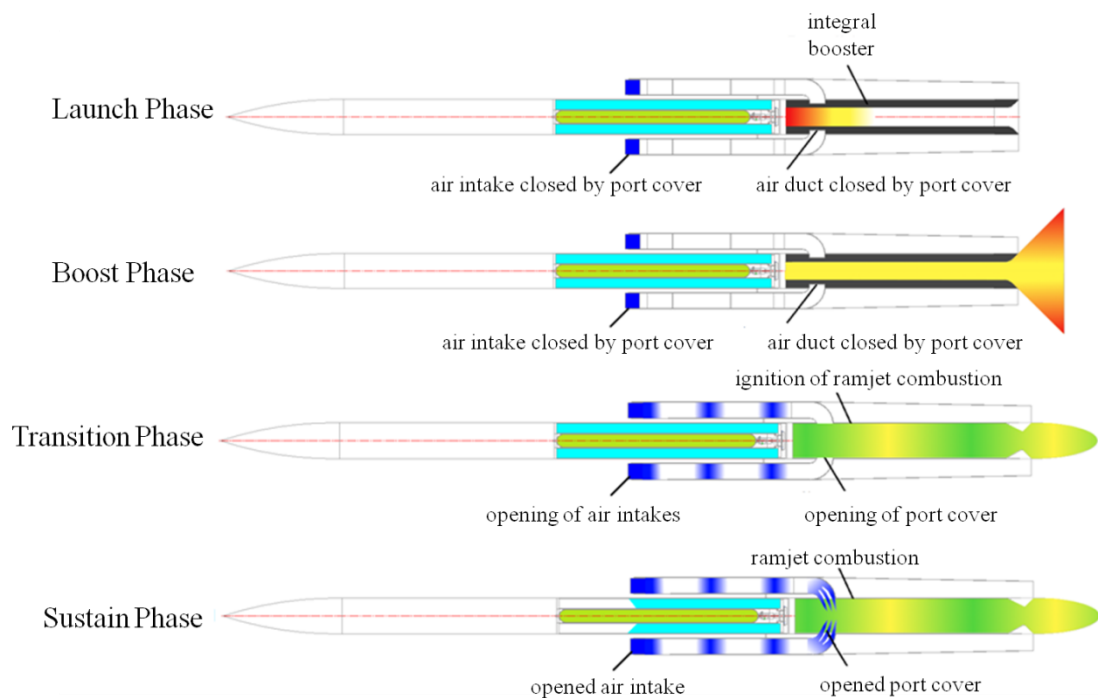


Figure 2: Operational Sequence of Integral Rocket Ramjet Concept [1].

Ramjet and the booster motors need a throat to maintain the required pressure inside the motor. However, it is not possible to design a ramjet and SPRM that operates with the same throat area. Therefore, at the end of the boost phase, during the transition

phase, nozzle geometry of the ramjet engine has to appear. The possible options to provide two different nozzle throats for integrated motors are limited. Two concept choices for an IRR system are booster with ejectable nozzle, and nozzleless booster.

1.1.1. Ejectable Nozzle

Ejectable nozzle is one of the concept choices for an IRR system. As the name suggests, nozzle of the booster is ejected at the end of its operation. Beneath the ejected part, nozzle geometry for the ramjet operation is preferred to exist.

It has been mentioned by Procinsky and McHale [3], ejectable nozzle approach has been proposed, demonstrated in ground tests and in a fewer number of flight tests. However, an ejectable nozzle assembly, shown typically in Figure 3, caused number of problems and performance penalties for the ramjet. Leakage between ejectable nozzle and the ramjet nozzle, difficulties to support mechanism structurally, malfunctions of the separation mechanism were the general reliability concerns. Nonetheless, ejectable nozzle concept was considered as most practical system. Herewith, most of the problems related have been solved. However, the risk of collision between ejected solid nozzle from the missile and the launching aircraft still remains.

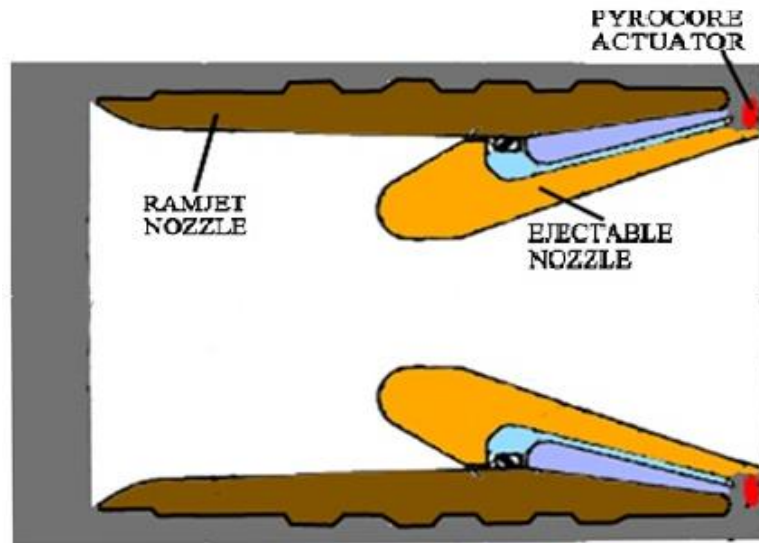


Figure 3: Ejectable Nozzle Assembly [3].

1.1.2. Nozzleless Solid Propellant Rocket Motor

Because of the serious functional problems of ejectable nozzle, design studies for nozzleless SPRM started in 1970s [4], [5].

As the name implies, nozzleless rocket motors are distinguished from the conventional rocket motors by the absence of nozzle. The idea of nozzleless rocket motor comes from its advantages against ejectable nozzle for an integral rocket ramjet type propulsion system. Main advantages of the nozzleless SPRMs compared to conventional ones are [4], [6]–[9].

- no moving parts
- less control circuits and actuators
- simpler propellant grain geometry
- larger volumetric loading
- reduced weight
- reduced price

- enhanced reliability because of the absence of a conventional nozzle
- ejection of the nozzle is not necessary

On the other hand, the main disadvantages can be summarized as :

- Around 20% deficiency in the specific impulse compared to conventional motors
- Possibility of having combustion instabilities at low pressures
- Wide range burn rate mapping of the propellant is required to predict the motor performance
- Mechanical deformations affect the internal ballistics of the motor directly
- Thrust vectoring is not possible.

Although most of these disadvantages can be solved during the design phase, lower specific impulse is the main drawback for the advantages. Reasons for lower specific impulse are the absence of a conventional converging-diverging nozzle, the immensely regressive pressure-time profile, and the decreased residence time of combustion gases due to high flow velocity inside the motor. However, more propellant can be placed due to absence of nozzle which can compensate the lower specific impulse in terms of total performance.

1.2. LITERATURE SURVEY

Although the nozzleless SPRM concept was revived 1970's, there is limited information in open literature, and most of it is directly related to future of integrated rocket ramjet concept for new generation air to air tactical missiles.

Internal ballistics numerical simulations can be classified by means of their dimensional modeling type of flow field.

- 0-Dimensional quasi steady flow field models
- Quasi 1-Dimensional unsteady and quasi steady flow field models
- 2-Dimensional, 3-Dimensional unsteady flow field models

0-Dimensional models, or lumped parameter models, are easy to apply and may provide useful results especially for conventional rocket motors. However, due to lack of flow information along the grain port, such models do not allow calculation of burning rate enhancement due to erosive burning.

Quasi 1-dimensional models allow more accurate analysis of SPRMs relative to 0-dimensional models. For conventional rocket motors, 1-dimensional methods give promising results in terms of performance prediction and ignition transient phase [10]–[14]. Although the more complete modeling of flow field inside the motor can be constructed using 2 or 3 dimensional unsteady flow assumption, solutions of these equations are computationally expensive. Moreover, results to predict performance of motor in terms of head-end pressure and thrust history of motor can be obtained with 1-dimensional models [15]. These types of models may be required to examine jet features and flow behavior during very unsteady phases of operation.

During the design and development of SPRMs, as the internal ballistics prediction capabilities improve, the reliability of the SPRM can increase and the reduction of the design and development costs can be obtained. Most of the companies and institutes, work on SPRM design and development, have their own models and simulations tools, which are considered as secret [15].

Harry [5] reviewed the differences between experimental evaluation and computer simulations of nozzleless motors. Their computer program calculates the gas flow in the port using one-dimensional frictionless continuity, momentum, energy, and state equations. More than ten different erosive burning correlations were tried. Erosive

burning correlations consisted of several empirical parameters. To determine those parameters, trial and error procedure was applied from motor firing data. They have demonstrated that their results were in good agreement with motor firing data.

Nahon [16] summarized some theoretical analysis to predict the performance of nozzleless SPRM comparing the results with the experimental data. In his theoretical work, he applied two models for burning rate calculations. First one was a simple one in which burning rate was assumed to be constant along the grain. He commented on that there was a balance between the decreasing normal burning rate along the grain due to decreasing pressure, and enhancing effect of erosive burning due to increasing gas flow velocity along the grain. The other model stated to be one dimensional flow solver with steady state equations allowing geometry evaluation. It included linear erosive burning law where law consisted of two empirical constants. He concluded that the prediction of pressure and thrust of nozzleless SPRMs is very susceptible to input data compared to conventional SPRMs.

Liou and Lien [17] performed a numerical analysis to study injection driven cold flows in a nozzleless solid SPRM. They have used finite volume technique to solve the 2-Dimensional Navier-Stokes equations without subgrid-scale turbulence models. They examined the variation of mean static pressure and axial velocity along the grain and compared them with existing experimental results. They concluded that numerical simulations are in well agreement with the experimental data.

Gany and Aharon [8] have made experimental and numerical analysis for the internal ballistics considerations of nozzleless rocket motors. Their theoretical analysis was based on quasi steady state one dimensional flow of a perfect gas for a constant port area along the grain. One of the main assumptions of this work was to consider the burning rate along the grain port constant. Physical reason behind this idea is the fact that erosive and pressure dependent burning contributions are able to compensate each

other. They tested directly the validity of this assumption of a uniform burning rate along the grain. Their measurements showed that burning time of head end section is approximately 1% shorter than that of the downstream section. Furthermore, their numerical results have been in well agreement with the experimental results in terms of pressure distribution along the port and maximum head end pressure. In the same work they have examined, by test, the effect of aft end geometry or exit cone on specific impulse. Different motor configurations with various cone lengths and expansion angles were fired. Main result deduced from these tests is for a same overall length and inner diameter of grain, increasing cone length drops the average pressure and leads to higher specific impulse losses but exit cone may improve the performance if the reduction of burning area before the choking location is insignificant relative to the overall burning area.

Krishnan and Ramakrishnan [4] used one dimensional numerical scheme to predict the performance of a nozzleless solid propellant rocket motor. In their numerical simulations it is assumed that the flow is one dimensional, quasi steady state, adiabatic and frictionless perfect gas. Erosive burning effects were modeled by using Lenoir and Robillard (LR) equation. LR erosion model is widely used model to calculate the burning rate for conventional SPRMs. Although this erosion model is to predict motor performance with erosive burning under subsonic cross flow conditions, it has been assumed that the equation is applicable for transonic and supersonic cross flow velocities. In order to estimate the constant coefficients in the model, they applied semi empirical procedure for the propellant used in the experimental motor firings. They compared the pressure, and thrust histories of numerical simulations and experimental data. It was concluded that their predictions are in acceptable agreement with the experimental results.

Krishnan and Rajesh [18] conducted experimental and numerical study to determine the erosive burning contribution to the burning rate under transonic and supersonic

cross flow Mach numbers. They have concluded that the increasing pressure and cross flow velocity enhances the erosive burning effect. Moreover, their experimental results show that the lower normal burning rate propellants are much more prone to be effected by erosive burning than those with higher normal burning rates. Additional, numerical analysis were done using one dimensional, quasi steady, inviscid flow with instantaneous mass addition of combustion gases that obey the perfect gas law and LR burning rate relation was used. They have obtained good match with experiments by trial and error fitting of erosive burning model parameters.

Kumar, Raghunandan and Kawakami [9] worked on dual-thrust nozzleless motors. They examined the flow features inside a grain port with narrow head end, wide aft end, and vice a versa. Main aim of their study was to capture the shock formation, and choking points of flow. They carried out numerical study with a fully implicit finite volume scheme of the compressible, Reynolds-Averaged, two-dimensional Navier-Stokes equations. They used k-omega turbulence model and noted that experienced some difficulties to converge the solution. They have commented that the shock formation inside the flow and high degree of coupling between the velocity, density, pressure and energy, due to nature of problem, lead to instability in the solution process.

John et. al. [6] have performed numerical studies to examine the intrinsic flow physics related to fluid-throat effect for nozzleless propulsion. They have used the same numerical scheme with Kumar et. al[9]. Due to convergence issues they were not be able to simulate continuous burning. As a result they carried out independent simulation for each time step after analytically predicting the recessed grain surface with the imposed burn rate law at each axial location and at each time interval.

Mikkelsen and Roys [19] have done numerical and experimental study on nozzleless SPRMs. For the numerical analysis, they developed one dimensional internal ballistics

computer program. To analyze the erosive burning effects, they applied the Saderholm erosion model and a model obtained from static firing tests of nozzleless motors. They compared the numerical results with these two different erosive burning models. In their own erosion model, 3 empirical constants exist and they used recommended values for these constants. In order to account for the combustion inefficiencies in their computer code, they have used reduced 95% reduced value of flame temperature of theoretical value. Their comparison with the experimental results have shown that, although the Saderholm erosion model has been developed for conventional nozzled rocket motors, both erosion models are capable of predicting performance of a nozzleless rocket motor. In the document, they have only given the head-end pressure prediction-test comparison. However, they have noted that the both erosion model give better head-end pressure predictions than thrust prediction. Main conclusion from the study is that the Saderholm erosion model is indirectly confirmed to describe erosive burning at Mach numbers greater than 0.5. In this study, parametric studies have been conducted as well, using a numerical scheme, including the effect of grain geometry and propellant burn rate.

As it can be seen in literature, performance prediction of nozzleless SPRMs with one-dimensional frictionless adiabatic flow solvers with appropriate erosion models are promising. Moreover, erosion models developed for conventional SPRMs can be used also to have good agreement with experimental results. However, erosion model seems to be supported by experimental data to determine the empirical coefficients. In light of this information, literature review has been extended to on erosion models. It has been noticed that Mukunda and Paul [20] developed universal erosive burning model for conventional SPRMs considering range of different propellants varying energy levels and different burn rates. They have concluded that their hypothesis, which claims that relations ship between erosive burning rate ratio, non-dimensional mass flux, and the Reynold's number based on the non-erosive burn rate and port diameter can be tied up. Therefore, they have come up with a universal model, to

calculate burn rate with erosive burning effect, which was claimed to have 10% accuracy for most practical propellants.

1.3. SCOPE OF THE THESIS

The purpose of this study is to develop an internal ballistics computer program to predict performance of Nozzleless SPRMs for entire combustion of the propellant in order to be used during design and development phase of Nozzleless SPRMs.

Developed computer program is appropriate to solve flow field inside cylindrical perforated grains, which are most common type of grain for nozzleless SPRMs. Numerical simulations have been conducted using one dimensional Euler flow model with mass addition. Quasi one dimensional approach has been applied. Solution algorithm is verified by typical shock tube problem. Computer program is validated with results of experimental data given by [4]. After the program's performance prediction capabilities are obtained, parametric studies are conducted to examine the effects of propellant grain shape and burning rate relation on the performance of motor.

1.4. CONTENT OF THE THESIS

In Chapter 2, a background information of nozzleless SPRMs are introduced. Firstly, fundamentals of nozzleless SPRMs are explained including main parts of them and internal ballistics. Secondly, methods related to internal ballistics prediction are explained.

Chapter 3 contains the detailed description of the internal ballistic computer program. The main assumptions, models and governing equations of the computer program are given in this chapter.

In chapter 4, validation of computer program with shock tube problem and experimental motor firing data is presented.

In chapter 5, parametric studies are conducted to see the effect of different design parameters on nozzleless solid propellant rocket motor performance.

CHAPTER 2

NOZZLELESS SOLID PROPELLANT ROCKET MOTORS

2.1. FUNDAMENTALS OF NOZZLELESS SPRM

2.1.1. Main Parts of Nozzleless SPRM

Main parts of nozzleless SPRMs are very similar to conventional ones except the nozzle. They consist of igniter, motor casing, propellant or grain, liner, insulator and preferably exit cone. A typical schematic diagram is given in Figure 4.

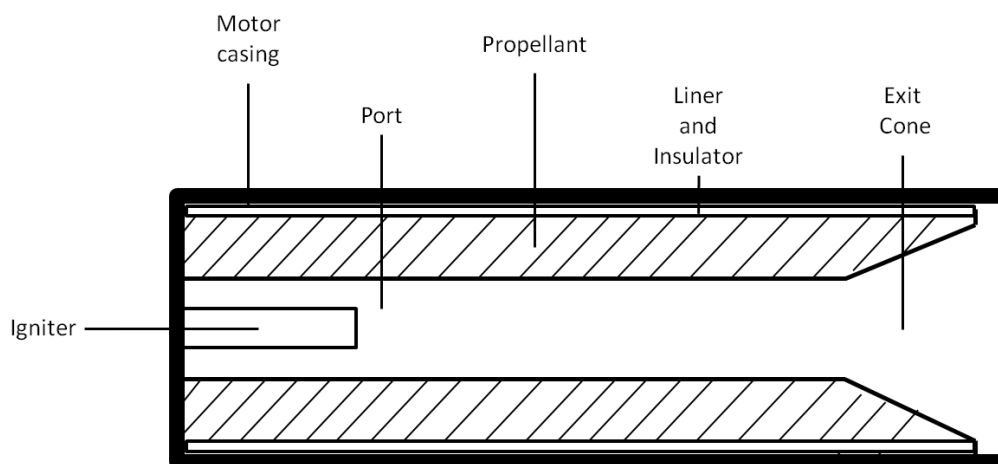


Figure 4: Schematic diagram of a nozzleless SPRM [4]

The main components and their functions are explained as follows :

a) Igniter: Main mission of the igniter is to initiate the ignition of propellant. They usually consists of primary charge or the booster charge, which is electrically ignited by initiator, and a larger secondary charge or the main charge, which is ignited by primary charge and ignites the solid propellant grain [21].

b) Motor casing: Motor casing is the structural element that holds other parts of SPRM. It is combustion chamber of SPRM as well due to the fact that combustion process occurs inside the casing. Moreover, for the integral rocket ramjet concept, after the solid propellant dies out and ramjet operation starts, the casing is used as combustion chamber of ramjet engine. Casing has to resist the thermal and pressure loads due to combustion. It is mainly a cylindrical thin walled pressure vessel; its thickness must be calculated considering the stresses due to pressure and temperature. They are usually used with thermal insulation. High strength metals like high resistance steels or composite materials like glass, Kevlar, carbon are used [21].

c) Propellant grain: Solid propellant is a fuel oxidizer mixture in solid state. Solid propellants are categorized by their chemical composition as double base and composite propellants.

Composite propellants are more commonly preferred type of propellants in SPRMs. It is mainly a heterogeneous mixture made of several kinds of substances. Most commonly used oxidizer is ammonium perchlorate. As a plastic binder and fuel Hydroxyl Terminated PolyButadiene (HTPB) is widely used.

Double base propellants are another category of solid propellants. In order to have this propellant, two kinds of base propellants are mixed. Contrary to composite propellants, chemical binding exist between the oxidizer and fuel.

Solid propellant that is cast in a special geometric form is called propellant grain. It is the main energy source for the propulsion and generates combustion gases with high temperature. Gases fill the port, and for an adequate length to diameter ratio of the port, naturally choked flow occurs due to continuous mass addition if enough pressure is satisfied inside the port. If sonic conditions are reached just before the exit cone, expansion occurs along it and gases are discharged with supersonic velocity [6].

To have a comparable performance relative to conventional SPRM, for a nozzleless, motors propellant properties have to be superior than used in conventional ones [3]. In order not to have inefficient thrust, burning rate has to be relatively higher. Furthermore, strain capacity of the propellant at low temperature should be high to have better volumetric loading and higher total performance. High stress capacity at high temperature is required, as well, to resist shear loads generated by the large axial pressure difference along the grain.

d) Insulation and liner : Combustion temperature of solid propellants is approximately between 1500 and 3500 K [21], which makes usage of thermal protection inevitable on interior surface of the case. Insulation is used to protect to case from the sustained thermal environment inside the motor. Moreover, it is used to relieve the case bond stresses between the case and propellant by providing shear layer [22]. Insulation thickness may vary along the case and is determined by considering the exposure time of the hot cases. Insulation is installed into the motor casing before the liner, which is applied on the insulation just before the propellant casting. Main duty of the liner is to provide bond coherence between the solid propellant and case.

2.1.2. Internal Ballistics of SRPM

Internal ballistics characterizes the motor behavior, performance, and mission capabilities. It can be examined by studying the internal flow conditions inside a SRPM covering all its operative conditions, from ignition to die out.

2.1.2.1. *Ballistics Parameters of the Nozzleless SRPMs*

a) Thrust: It is the force generated by propulsion system acting on a flight vehicle. Thrust generated by a rocket engine can be found from the momentum equation as follows :

$$F = \dot{m}V_e + (p_e - p_0)A_e \quad (2-1)$$

Where F describes the thrust, \dot{m} being mass flow rate discharged from the motor, V_e is the discharged gas velocity, p_e is the discharged gas pressure and A_e is the exit area for discharged gases. p_0 represents the ambient pressure.

b) Chamber Pressure: Pressure inside the port or combustion chamber during the operational time of the motor is called chamber pressure. During the design procedure, there is usually an upper limit to chamber pressure. According to the motor design, structural components are designed to resist to maximum limit pressure, and it is called as maximum expected operating pressure (MEOP)

Flow is accelerating along the grain port due to continuous mass addition. Therefore, static pressure drops as the Mach number increases. Maximum pressure occurs at the head end of the motor. Axial pressure difference generates loads on the grain, and propellant have to resist these loads.

c) Burning Rate: Propellant grain regresses in a direction perpendicular to the burning surface of the grain. This rate of regression is called burning rate and it is expressed in m/s . Generated mass flow rate due to burning can be calculated by :

$$\dot{m} = A_b r_b \rho_p \quad (2-2)$$

where A_b is the burning area, r_b is the burning rate and ρ_p is the solid propellant density.

There are several parameters that affect burning rate of the propellant. These are mainly pressure, temperature, burning rate enhancement due to erosive burning, and acceleration or spin induced grain stress. Vielle's or Saint Robert's law models the burning rate empirically and assumes that the burning rate is only function of local pressure.

$$r_b = a \left(\frac{p}{p_{ref}} \right)^n \quad (2-3)$$

where p represents the local pressure, p_{ref} is the reference pressure, a , and n are empirical constants. These constant are usually obtained from results of strand burner or Ballistic Evaluation Motor (BEM) tests. However, these empirical constants vary with temperature. The sensitivity of burning rate to propellant temperature can be defined as follows:

$$\sigma_p = \left[\frac{\partial \ln r_b}{\partial T} \right]_p \quad (2-4)$$

where σ_p describes the temperature sensitivity of burning rate expressed as percent change of burning rate per degree change in propellant temperature at a particular value of chamber pressure.

Burning rate enhancement due to erosive burning becomes important when there are high gas cross-flow velocities inside the port [23]–[26]. High cross flow velocity over the burning surface increases the heat transfer from the flame to the burning surface. In a nozzleless motor port, it is certain that sonic conditions will be reached for most of the operational time, and supersonic conditions can be seen along the exit cone. Therefore, erosive burning is an important parameter for the performance prediction of nozzleless motors. There are different erosive burning models in the literature developed for conventional SPRMs. Although the models have been developed for conventional SPRMs, in the literature [19],[4] these models have been used to predict performance of nozzleless SPRM. One of the models is called “Lenoir-Robillard” or LR erosion model which is used widely to predict [22], [26]–[28] performance of conventional SPRMs. According to LR model burning rate is defined as :

$$r_b = r_0 + r_e \quad (2-5)$$

where r_0 is the normal burning rate which is defined by Saint Robert’s law as follows:

$$r_0 = a \left(\frac{p}{p_{ref}} \right)^n \quad (2-6)$$

p with being the local pressure, and p_{ref} being the reference pressure, it is usually taken to be 1 bar. r_e in equation (2-5) is the burning rate contribution from erosive burning and represented as:

$$r_e = \frac{\alpha G^{0.8}}{L_x^{0.2}} \exp\left(-\frac{\beta \rho_p r_b}{G}\right) \quad (2-7)$$

where α and β are empirical constants, G is the mass flux, L_x is the local axial distance from the head end. However, it is proposed that L_x can be modified as local hydraulic port diameter [16].

d) Specific Impulse: Measure of momentum change produced per unit mass of propellant consumed is called specific impulse, I_{sp} . It can be defined as the ratio of the thrust to the propellant weight flow rate and the unit of specific impulse is seconds. It can be calculated as follows :

$$I_{sp} = \frac{F}{\dot{m}g} \quad (2-8)$$

In this equation g is the standard gravitational acceleration.

e) Total Impulse : It is defined as the integration of thrust over the operational time of the motor and is calculated as:

$$I_{tot} = \int_0^{t_b} F dt = \bar{F} t_b \quad (2-9)$$

where I_{tot} is the total impulse, t_b is the operation time of the motor, and \bar{F} is the average thrust over the operation time. It can be calculated integrating the area under the thrust-time curve. It directly indicates the total energy generated by all the propellant to produce thrust.

f) Volumetric Loading Fraction: It is defined as the ratio of the propellant volume to the available chamber volume.

g) Web Fraction: The ratio of the propellant thickness to the outer radius of the grain is called web fraction. Thickness of the propellant is called “web thickness” as well.

2.1.2.2. *Temporal Phases of Operation*

Operating time of a SPRM can be divided into three major phases. These can be identified by considering the relation between thrust-time or pressure-time as: Ignition Transient, Quasi-Steady State and Tail-off as given in Figure 5. Characteristics of these phases are described below.

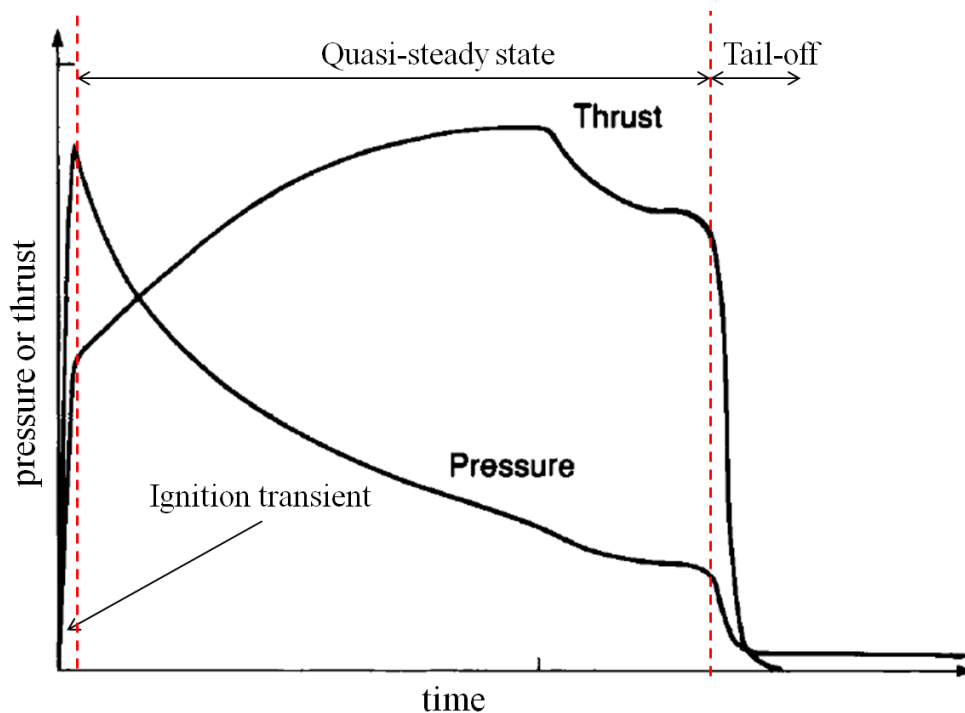


Figure 5: Typical thrust-pressure curves of a nozzleless propellant grain [17]

2.1.2.3. *Ignition Transient*

Ignition transient phase is the first temporal phase of motor operation. It starts as the ignition signal is sent to igniter, ends when the motor fills with combustion gases, and balance between the generated and discharged gases are reached.

After the signal is received by the igniter, it is fired and gases impinge on propellant surface which starts the ignition of grain propellant which is called “induction interval”. Afterwards, flame spreading triggers the ignition of the entire grain during the so called “flame spreading interval”. Lastly, grain burning surface completely ignites, chamber fills, and quasi steady state conditions are achieved in the chamber [15].

2.1.2.4. *Quasi Steady State*

Quasi steady state phase starts at the end of ignition transient phase and generally it is the longest phase of operation. Ultimate and efficient thrust is achieved during this phase. Moreover, motor is expected to satisfy its performance requirements at the end of quasi steady state phase.

During this phase, internal ballistics is driven by mass addition due to grain burning, time history of mass addition and variation of combustion gases and grain burning surface regression. For conventional rocket motors, although nozzle throat area increases due to ablation it is not significant as for the case of nozzleless motor. Due to absence of nozzle, the naturally choked flow occurs inside the grain, where the mass flux is maximum. Port area at the fluid throat increases according to the burn rate of propellant which is significantly larger than ablation rate of a conventional nozzle. Therefore, chamber pressure profile is highly regressive (Figure 5) and thrust profile depends on the burning rate characteristics of propellant.

2.1.2.5. Tail Off

Tail off phase starts at the end of quasi steady state phase. It is identified by sudden drop of pressure or thrust.

Because of the grain surface regression, larger parts of the insulator or liner are exposed to the combustion gases and effective burn area of propellant decreases. Lower burn area results in smaller mass addition of combustion products and chamber pressure drops suddenly. Poorly designed nozzleless rocket motors may experience pressure fluctuations or chuffing and long and inefficient tail-off [8]. As a result, tail-off phase is identified by unsteady phenomenon according to chamber pressure drop, combustion stability and thermal insulation or liner ablation.

2.2. INTERNAL BALLISTICS PREDICTION AND ANALYSIS

Internal ballistics numerical simulations can be classified by means of their dimensional modeling type of flow field as follows:

- 0-Dimensional quasi steady flow field models
- Quasi 1-Dimensional unsteady and quasi steady flow field models
- 2-Dimensional, 3-Dimensional unsteady flow field models

2.2.1. 0-Dimensional Quasi Steady Flow Field Models

It is a simple modeling of the internal ballistic and named as 0-dimensional models or lumped parameter, volume-filling models [9]. For this analysis, mass flow of gas at constant temperature is assumed to being pumped into a volume that change over time. Concurrently, some mass flow of gas exits from the volume. By applying the conservation of mass and energy in the volume change of pressure and temperature inside the chamber can be calculated.

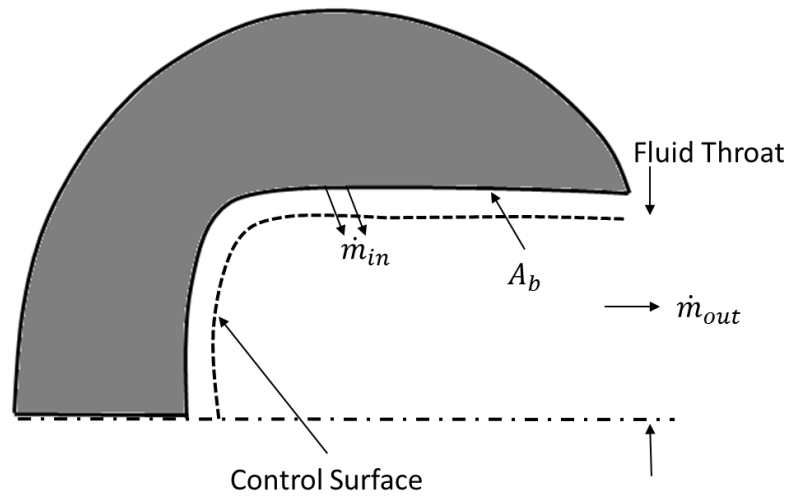


Figure 6: 0-Dimensional Lumped Parameter Analysis.

In order to calculate the outflow rate, Mach number at fluid throat has to be known. For a nozzleless SPRM it can be assumed that choking condition is satisfied at the aft end of grain geometry unless there is an exit cone. Inflow rate is found by using a burning rate relation, total burn area and density of solid propellant.

For an unknown choking location and properties, application of these types of models is not possible.

2.2.2. 1-Dimensional Quasi-steady and Unsteady Analysis

In order to have a more accurate analysis of nozzleless SPRMs internal ballistics, which are by design have high length to diameter ratio and gas flow with sonic and supersonic features inside the grain port, one dimensional models are required. These types of models describe the flow field properties as dependent on axial position along the motor axis and time. For quasi steady models, flow field is assumed to be constant for a defined time interval and conservation equations are used without transient terms. On the other hand, unsteady models allow solving ignition transient phase of the

operation as well. Igniter models, ignition criteria and heat transfer models can be implemented in these types of models.

Burning rate can be modeled much more accurately than 0-dimensional models. Most of the erosion models given in literature are appropriate to be used with one-dimensional models. These models allow examining the grain surface regression at different axial locations which is an important feature especially to trace the regression of fluid throat and exit cone to predict performance.

2.2.3. 2-Dimensional Unsteady Flow Field Models

For conventional SPRMs 3-dimensional modeling of flow field is used as well. However, it has been not found any 3-dimensional flow field model for nozzleless SPRMs during the literature review. This may be due to the fact that grain port geometries of most nozzleless motors are cylindrical and axisymmetric.

A general and more complex modeling of a port flow with 2-dimensional Navier-Stokes equations gives more detailed results than 1-dimensional model to examine the flow features inside the motor. Detailed modeling of igniter jets, modeling of flame propagation can be possible. On the other hand, they are computationally expensive and accuracy of results in terms of head-end pressure time history can be achieved with 1-dimensional models as well [9].

In order to have complete simulation of internal ballistic over ignition transient, quasi steady state and tail-off some problems have to be solved. One of the difficulties is the fact that as the grain burning surface regresses, the computational domain changes and updated bore geometry must be accounted in the flow solver which requires a complex coupling between the grid of the grain and the main flow field.

CHAPTER 3

COMPUTATIONAL METHODOLOGY

In this chapter, internal ballistics computer program developed for nozzleless solid propellant rocket motors will be presented.

3.1. GAS DYNAMICS MODEL

Numerical simulations are conducted solving one dimensional Euler equations with mass addition. Quasi one dimensional approach is used. In this approach it is assumed that :

- Internal flow is quasi one-dimensional,
- There are not any heat or viscous losses,
- Mass addition is an instantaneous process,
- There is no momentum contribution parallel to the motor axis due to the mass addition from burned grain surface,
- Grain regression is in radial direction only

Grain port is divided into finite number of cells or slices and conservation equations are applied to each (Figure 7).

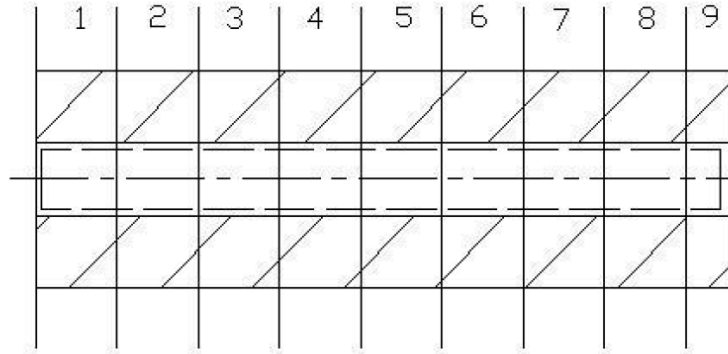


Figure 7: Slices of Grain Port.

Indexing for adjacent cells, control volume, and cell faces is shown in Figure 8.

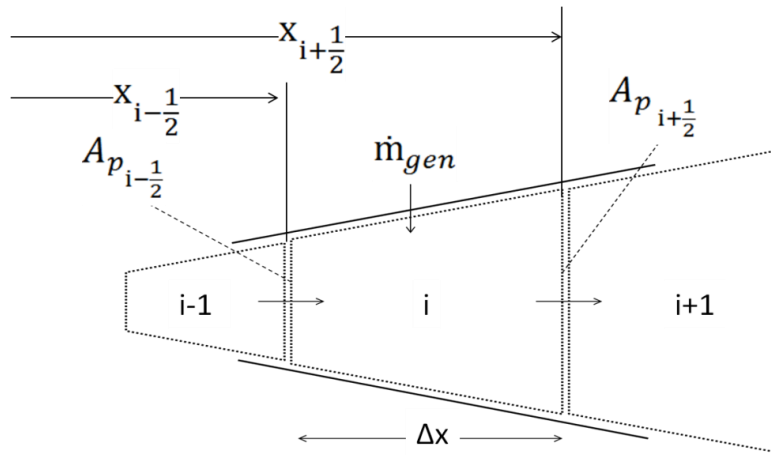


Figure 8: Control Volume for one-dimensional model

Conservation of mass, momentum and energy is applied along the slices for each cell. If it is denoted as; ρ is fluid density, u is axial fluid velocity, A_p is port area, p is fluid static pressure, E is total energy per unit mass, \dot{m}'_{gen} is generated mass per unit length due to the combustion of propellant, h_{prop} is total enthalpy of the combustion gases, x is the axial coordinate, and t is the time, general conservation equations are as follows:

Conservation of mass:

$$\frac{\partial(\rho A_p)}{\partial t} + \frac{\partial}{\partial x}(\rho u A_p) = \dot{m}'_{gen} \quad (3-1)$$

Conservation of momentum:

$$\frac{\partial(\rho u A_p)}{\partial t} + \frac{\partial}{\partial x}[(\rho u^2 + p)A_p] = p \frac{\partial A_p}{\partial x} \quad (3-2)$$

Conservation of energy:

$$\frac{\partial(\rho e A_p)}{\partial t} + \frac{\partial}{\partial x}[(\rho E + p)u A_p] = \dot{m}'_{gen} h_{prop} \quad (3-3)$$

In these equations, terms on the right hand sides represent the source terms. Using a solution vector \mathbf{q} , flux vector \mathbf{F} , and source vect

or \mathbf{S} as follows :

$$\mathbf{q} = \begin{bmatrix} \rho \\ \rho u \\ \rho E \end{bmatrix}, \mathbf{F} = \begin{bmatrix} \rho u \\ \rho u^2 + p \\ (\rho E + p)u \end{bmatrix} \text{ and } \mathbf{S} = \begin{bmatrix} \dot{m}'_{gen} \\ p \frac{\partial A_p}{\partial x} \\ \dot{m}'_{gen} h_{prop} \end{bmatrix} \quad (3-4)$$

and the three conservation equations can be represented shortly in the following form:

$$\frac{\partial(\mathbf{q}A_p)}{\partial t} + \frac{\partial(\mathbf{F}A_p)}{\partial x} = \mathbf{S} \quad (3-5)$$

If discrete coordinates are defined for each cell interface as shown in Figure 8, discrete spacing between two cells interface, Δx for the i th cell can be written as follows:

$$\Delta x_i = x_{i+\frac{1}{2}} - x_{i-\frac{1}{2}} \quad (3-6)$$

and the discrete time interval of solution can be defined as :

$$\Delta t^j = t^{j+1} - t^j \quad (3-7)$$

Therefore, equation (3-5) can be approximated as follows :

$$\frac{[qA_p]_i^{j+1} - [qA_p]_i^j}{\Delta t} + \frac{[FA_p]_{i+\frac{1}{2}}^j - [FA_p]_{i-\frac{1}{2}}^j}{\Delta x_i} = S \quad (3-8)$$

To find the cell center variables for the next time step is calculated as :

$$(qA_p)_i^{j+1} = (qA_p)_i^j - \frac{\Delta t}{\Delta x_i} \left[(FA_p)_{i+\frac{1}{2}}^j - (FA_p)_{i-\frac{1}{2}}^j - S\Delta x_i \right] \quad (3-9)$$

In equation (3-4) \dot{m}'_{gen} is the generated mass source per unit length in a related control volume and defined as:

$$\dot{m}'_{gen} = \frac{\dot{m}_{gen}}{\Delta x_i} \quad (3-10)$$

And the derivative of port area with respect to axial distance can be calculated by first order approximation as follows:

$$\frac{\partial A_p}{\partial x} = \frac{\left(A_{p_{i+\frac{1}{2}}} - A_{p_{i-\frac{1}{2}}} \right)}{\Delta x_i} \quad (3-11)$$

ρA_p , $\rho u A_p$ and $\rho e A_p$ for the next time step can be represented as follows:

$$(\rho A_p)_i^{j+1} = (\rho A_p)_i^j - \frac{\Delta t}{\Delta x_i} \left[(\rho u A_p)_{i+\frac{1}{2}}^j - (\rho u A_p)_{i-\frac{1}{2}}^j - \dot{m}_{gen} \right] \quad (3-12)$$

$$\begin{aligned} (\rho u A_p)_i^{j+1} &= (\rho u A_p)_i^j \\ &\quad - \frac{\Delta t}{\Delta x_i} \left[[(\rho u^2 + p) A_p]_{i+\frac{1}{2}}^j - [(\rho u^2 + p) A_p]_{i-\frac{1}{2}}^j \right. \\ &\quad \left. - p_i \left(A_{p_{i+\frac{1}{2}}} - A_{p_{i-\frac{1}{2}}} \right) \right] \end{aligned} \quad (3-13)$$

$$\begin{aligned} (\rho e A_p)_i^{j+1} &= (\rho e A_p)_i^j \\ &\quad - \frac{\Delta t}{\Delta x_i} \left[[(\rho E + p) u A_p]_{i+\frac{1}{2}}^j - [(\rho E + p) u A_p]_{i-\frac{1}{2}}^j \right. \\ &\quad \left. - \dot{m}_{gen} h_{prop} \right] \end{aligned} \quad (3-14)$$

The set of equations are closed by equation of state. For most case, compressible gas can be assumed to be ideal or perfect gas. Therefore, equation of state is written as follows:

$$p = \rho RT \quad (3-15)$$

where T is the temperature, and R is the gas constant, found by dividing the universal gas constant, \bar{R} , to molecular weight of the gas. Universal gas constant is taken to be [29] :

$$\bar{R} = 8.3145 \frac{kJ}{kmol K} \quad (3-16)$$

Total energy per unit mass, E , is defined as follows :

$$E = e + \frac{1}{2}u^2 \quad (3-17)$$

with e is being internal energy and for a calorically perfect gas it can be defined in terms of pressure and density as follows :

$$e = \frac{1}{\gamma - 1} \frac{p}{\rho} \quad (3-18)$$

where γ represents the ratio of specific heats. Thus, E can be written as follows :

$$E = \frac{1}{\gamma - 1} \frac{p}{\rho} + \frac{1}{2}u^2 \quad (3-19)$$

Thus, only unknown left is the generated mass flow due to combustion of propellant. To find the amount of mass flow source for each cell, equation (3-20) is used.

$$\dot{m}_{gen} = r_b A_b \rho_p \quad (3-20)$$

Where, r_b is the local propellant burning rate, A_b is the total burning area of the related cell slice and ρ_p is the solid propellant density. Port area, A_p for the next time step is found using the local propellant rate. For a cylindrical shape port area can be calculated as :

$$A_p = \pi r^2 \quad (3-21)$$

r is the port radius and port radius for the next time step is simply found by :

$$r^{j+1} = r^j + r_b \Delta t \quad (3-22)$$

In order to calculate the both generated mass flow and port radius for the next time step, burning rate have to be calculated.

3.2. BURNING RATE RELATION

In order to predict the local burning rate for each cell, effect of pressure and erosive burning is considered, and universal erosive burning relation given by Mukunda and Paul [20] is used. According to this relation total burning rate is defined as :

$$r = \eta r_0 \quad (3-23)$$

where r_0 is the normal burn rate which is defined by Saint Robert's law as:

$$r_0 = a \left(\frac{p}{p_{ref}} \right)^n \quad (3-24)$$

with p being the local pressure in bars and p_{ref} is taken to be 1 bar. Erosive burning coefficient, η , is found as follows :

$$\eta = 1 + K_1 (g^{0.8} - g_{th}^{0.8}) \mathcal{H}(g - g_{th}) \quad (3-25)$$

\mathcal{H} defines the Heaviside function. Mukunda and Paul [20] recommends values of $K_1 = 0.023$, $g_{th} = 35$. g in equation (3-25) is calculated as follows :

$$g = g_0 \left(\frac{Re_0}{1000} \right)^{-\frac{1}{8}} \quad (3-26)$$

where g_0 and Re_0 are calculated as follows :

$$g_0 = \frac{G}{\rho_p r_0} \quad , \quad Re_0 = \frac{\rho_p r_0 d_h}{\mu} \quad (3-27)$$

where, G is the mass flux, d_h is the hydraulic diameter, μ is the dynamic viscosity, and ρ_p is the solid propellant density. Mass flux for the i th cell is calculated as follows:

$$G = \rho_i u_i \quad (3-28)$$

3.3. FLUX SPLITTING SCHEME

In this part calculation scheme for the flux vector \mathbf{F} at the cell interface is given.

In the literature, various schemes to calculate fluxes are proposed and examined for the Euler equations [30]–[35]. Most of the schemes used, to solve Euler equations, depend on first order upwind differencing. These schemes can be categorized as flux difference splitting, and flux vector splitting. Flux difference splitting methods use approximate solution of the local Riemann problem, while the flux vector splitting methods separate the flux vector into upstream and downstream components. One of the most successful and well known methods is Roe's approximate Riemann method [35]. This method can capture stationary discontinuities without any numerical dissipation. However, nonphysical expansion shocks may be generated and at strong expansions, solutions may diverge [36].

In the flux vector splitting approach, \mathbf{F} , which is function of the \mathbf{q} vector given by (3-4), is separated into positive and negative contributors as follows:

$$\mathbf{F}(\mathbf{q}) = \mathbf{F}^-(\mathbf{q}) + \mathbf{F}^+(\mathbf{q}) \quad (3-29)$$

The flux at cell interface between right and left states (Figure 9) is represented as:

$$\mathbf{F}_{1/2}(\mathbf{q}_L, \mathbf{q}_R) = \mathbf{F}^+(\mathbf{q}_L) + \mathbf{F}^-(\mathbf{q}_R) \quad (3-30)$$

A well known flux splitting method was proposed by Steger and Warming [37] which generates errors around the sonic locations of the flow field. However, for the present calculations to solve internal flow field of nozzleless motor, determination of choking point and flow properties there is critical. Another flux splitting scheme was introduced by Van Leer [38] which behaves better than Steger-Warming method in

terms of solving sonic points. Nonetheless, this scheme is not suitable to capture contact discontinuities [39].

The scheme, Liou, Steffen presented and named as the Advection Upstream Splitting Method (AUSM) [40] solves the most problems of Steger-Warming and Van-Leer methods. Moreover, it is claimed to be as accurate as Roe's flux difference splitting scheme. However, oscillations at shocks are observed with AUSM scheme as well [41]. Wada and Liou [36] proposed improved version of AUSM scheme, named as AUSMDV scheme. This scheme is effective in taking out expansion shocks, glitches at sonic points and problems related to contact discontinuities. It is also known with its numerical efficiency and compatibility with chemically reacting flows. Therefore, AUSMDV scheme is chosen to be appropriate for the present study.

Left	1/2	Right
u_L		u_R
ρ_L		ρ_R
p_L		p_R
H_L		H_R

Figure 9: Adjacent Cells and the Interface

For the calculation of mass flow rate at cell interface between left and right cells shown in Figure 9, below equations is used.

$$(\rho u A_p)_{\frac{1}{2}}^n = (\rho u)_{\frac{1}{2}}^n (A_p)_{\frac{1}{2}}^n \quad (3-31)$$

Calculation of mass flux is represented as follows:

$$(\rho u)_{\frac{1}{2}} = U_L^+ \rho_L + U_R^- \rho_R \quad (3-32)$$

In order to calculate U_L^+ , left cell velocity is checked to see whether it is larger or smaller than the maximum speed of sound, c_m , of two adjacent cells in terms of magnitude as in equations (3-33) and (3-34).

$$U_L^+ = \alpha_L \left[\frac{(u_L + c_m)^2}{4c_m} \right] + (1 - \alpha_L) \frac{u_L + |u_L|}{2}, \quad \text{if } |u_L| \leq c_m \quad (3-33)$$

$$U_L^+ = \frac{u_L + |u_L|}{2}, \quad \text{if } |u_L| > c_m \quad (3-34)$$

Similar procedure is followed to calculate U_R^- as :

$$U_R^- = \alpha_R \left[-\frac{(u_R + c_m)^2}{4c_m} \right] + (1 - \alpha_R) \frac{u_R - |u_R|}{2}, \quad \text{if } |u_R| \leq c_m \quad (3-35)$$

$$U_R^- = \frac{u_R - |u_R|}{2}, \quad \text{if } |u_R| > c_m \quad (3-36)$$

where c_m is the maximum local speed of sound for adjacent cells which is found by comparing the speed of sound for left and right cells as :

$$c_m = \max(c_L, c_R) \quad (3-37)$$

And α_L and α_R are defined as:

$$\alpha_L = \frac{2 \left(\frac{p}{\rho}\right)_L}{\left[\left(\frac{p}{\rho}\right)_L + \left(\frac{p}{\rho}\right)_R\right]} \quad \alpha_R = \frac{2 \left(\frac{p}{\rho}\right)_R}{\left[\left(\frac{p}{\rho}\right)_L + \left(\frac{p}{\rho}\right)_R\right]} \quad (3-38)$$

For the second term of flux matrix, equation can be separated as follows :

$$[(\rho u^2 + p)A_p]_{\frac{1}{2}}^n = \left[(\rho u^2)_{\frac{1}{2}} + p_{\frac{1}{2}}\right] A_p \frac{1}{2} \quad (3-39)$$

For the first term of momentum flux, equation (3-40) is used.

$$(\rho u^2)_{\frac{1}{2}AUSMDV} = \frac{1}{2}(1 + s)(\rho u^2)_{\frac{1}{2}AUSMV} + \frac{1}{2}(1 - s)(\rho u^2)_{\frac{1}{2}AUSMD} \quad (3-40)$$

where s is defined as :

$$s = \min\left(1, \frac{K|p_R - p_L|}{\min(P_L, P_R)}\right) \quad (3-41)$$

where K is taken to be 10 as recommended in [36]. ρu^2 contributions for AUSMV and AUSMD are calculated as follows :

$$(\rho u^2)_{\frac{1}{2}AUSMV} = U_L^+(\rho u)_L + U_R^-(\rho u)_R \quad (3-42)$$

$$(\rho u^2)_{\frac{1}{2}AUSMD} = \frac{1}{2} \left[(\rho u)_{\frac{1}{2}}(u_L + u_R) - \left| (\rho u)_{\frac{1}{2}} \right| (u_R - u_L) \right] \quad (3-43)$$

For the pressure term in equation (3-39), following equation is used.

$$p_{\frac{1}{2}} = p_L^+ + p_R^- \quad (3-44)$$

where in order to calculate p_L^+ , left cell velocity is checked to see whether it is larger or smaller than the maximum speed of sound of two adjacent cells in terms of magnitude as follows :

$$p_L^+ = p_L \left[\frac{(u_L + c_m)^2}{4c_m^2} \right] + \left(2 - \frac{u_L}{c_m} \right), \quad \text{if } |u_L| \leq c_m \quad (3-45)$$

$$p_L^+ = p_L \left[\frac{(u_L + |u_L|)}{2u_L} \right], \quad \text{if } |u_L| > c_m \quad (3-46)$$

Similar procedure is followed to calculate p_R^- as :

$$p_R^- = p_R \left[\frac{(u_R + c_m)^2}{4c_m^2} \right] + \left(2 + \frac{u_R}{c_m} \right), \quad \text{if } |u_R| \leq c_m \quad (3-47)$$

$$p_R^- = p_R \left[\frac{(u_R + |u_R|)}{2u_R} \right], \quad \text{if } |u_R| > c_m \quad (3-48)$$

Lastly, for the enthalpy flux, E and h is defined as:

$$E = e + \frac{u^2}{2} \quad \text{and} \quad h = e + \frac{p}{\rho} \quad (3-49)$$

To find the total enthalpy per unit volume per unit mass equation

$$H = h + \frac{u^2}{2} = E + \frac{p}{\rho} \quad (3-50)$$

Therefore, energy flux can be represented as:

$$(\rho E + p)u = \rho u \left(E + \frac{p}{\rho} \right) = \rho u H \quad (3-51)$$

Enthalpy flux at the interface between adjacent cells is found as:

$$\rho u H_{\frac{1}{2}} = \frac{1}{2} \left((\rho u)_{\frac{1}{2}} (H_L + H_R) - \left| (\rho u)_{\frac{1}{2}} (H_R - H_L) \right| \right) \quad (3-52)$$

where total enthalpy for left and right cells are calculated as:

$$H_{L,R} = \frac{c_{L,R}^2}{\gamma - 1} + \frac{1}{2} u_{L,R}^2 \quad (3-53)$$

3.4. BOUNDARY CONDITIONS

One-dimensional solution domain is constructed with 2 boundary conditions (Figure 10). These boundary conditions are applied to extra cells, named ghost cells. These cells are not included in the real length of the motor, in other words source terms are not assigned to these cells. Location of boundary condition cells are given in Figure 10.

Wall BC					Outlet BC
1	2	i	imax-1	imax	imax+1

Figure 10: Cell numbering and boundary conditions.

Standart wall and outflow boundary conditions are applied as defined in [14], [41]–[43]. For wall boundary conditions, to interfere the mass transfer between the 1st and 2nd cell, all the properties are copied from the cell number 2 to cell number one except velocity. In other words, $\rho(1) = \rho(2)$, $u(1) = -u(2)$ and $E(1) = E(2)$ are applied.

For the outflow boundary condition, two different states are defined according to the Mach number of cell imax. If it is supersonic, all the variables are directly extrapolated to the (imax+1)th cell as :

$$\begin{aligned}
 \rho_{imax+1} &= \rho_{imax} \\
 u_{imax+1} &= u_{imax} \\
 E_{imax+1} &= E_{imax}
 \end{aligned}
 \tag{3-54}$$

If subsonic flow occurs at cell imax, then the following procedure is applied.

$$\begin{aligned}
\rho_{i_{\max}+1} &= \rho_{i_{\max}} \\
u_{i_{\max}+1} &= u_{i_{\max}} \\
P_{i_{\max}+1} &= P_{\text{out}} \\
E_{i_{\max}+1} &= \frac{P_{\text{out}}}{\gamma - 1} + \frac{1}{2} \rho_{i_{\max}+1} u_{i_{\max}+1}^2
\end{aligned} \tag{3-55}$$

with P_{out} being the input for calculations and represents the ambient pressure at the motor exit.

3.5. SOLUTION ALGORITHM

3.5.1. Unsteady Solution

Unsteady solutions are achieved following the below procedure:

1. Flow domain is initialized with the desired primitive variables (density, velocity, pressure) and using those primitive variables, conservative variables for each cell is calculated.
2. Local burning rate of propellant at each cell is found using appropriate burning rate according to cell variables relation. (Equations (3-23)-(3-28))
3. Mass source for the calculation of next time step is calculated according to local burning rates and burning area for each cell. (Equation (3-20))
4. With flux splitting algorithm, fluxes at the each interface between adjacent cells are calculated. (Equations (3-31)-(3-53))
5. Flow field is geometrically updated considering the local burning rates. (Equation (3-22))
6. Using calculated fluxes and source terms, conservative variables of each cell for the next time step is obtained. (Equations (3-12)-(3-14))

7. Procedure is repeated following the 2nd step until the calculation stops.

3.5.2. Quasi-Steady Solution

A quasi steady solution is accomplished using the following procedure:

1. Flow domain is initialized with the desired primitive variables (density, velocity, pressure) and using those primitive variables, conservative variables for each cell is calculated.
2. Local burning rate of propellant at each cell is found using appropriate burning rate according to cell variables relation. (Equations (3-23)-(3-28))
3. Mass source for the calculation of next iteration is calculated according to local burning rates and burning area for each cell. (Equation (3-20))
4. With flux splitting algorithm, fluxes at the each interface between adjacent cells are calculated. (Equations (3-31)-(3-53))
5. Using calculated fluxes and source terms, conservative variables of each cell for the next iteration is obtained. (Equation (3-22))
6. Procedure is repeated following the 2nd step until the solution converges for a defined times interval.
7. Flow field is geometrically updated considering the converged results of local burning rates. (Equation (3-22))
8. Procedure is repeated following the 1st step until the calculation stops.

CHAPTER 4

VALIDATION RESULTS

In this chapter, results obtained for the validation of the developed computer program will be presented. First of all, in order to validate the solution algorithm, shock tube problem is solved. Secondly, grid size sensitivity and time step size sensitivity study are presented. Third, to test the overall performance prediction capability of the code against some of the experimental nozzleless SPRMs [4] are simulated and the prediction results are compared with the experimental data. Comparison is done using the pressure and thrust histories, which are main performance parameters of a nozzleless SPRM. Lastly, detailed examination of predictions in terms of internal ballistics is presented.

4.1. SHOCK-TUBE CASE

In this section, verification of the transient quasi one dimensional flow solver against the Sod Shock tube problem is given. According to the problem, tube is initially divided into 2 sections, with different stationary flow variables, by a fictitious diaphragm at the middle as shown in Figure 11.

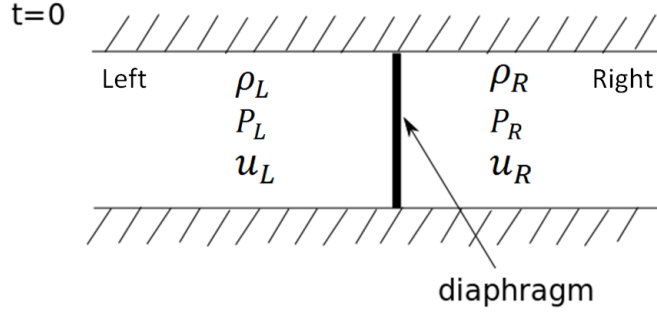


Figure 11: Initial Conditions for Sod Shock Tube Problem

At time is zero, diaphragm disappears and transient solutions start. Due to the fact that initially, flow variables at right and left side of the diaphragm are different, both expansion and shock waves occur and move. For the test case a 10 meter long tube is simulated. The initial values of flow variables at right and left side of the diaphragm are set as:

$$\begin{aligned}
 u_L = 0 \frac{m}{s}, \quad \rho_L = 1 \frac{kg}{m^3}, \quad P_L = 1 Pa, \quad & \text{if } x < 5 m \\
 u_R = 0 \frac{m}{s}, \quad \rho_R = 0.125 \frac{kg}{m^3}, \quad P_R = 0.1 Pa, \quad & \text{if } x \geq 5 m
 \end{aligned}
 \tag{4-1}$$

For the solutions different grid sizes (different number of total cells) are used. Time step is calculated for constant CFL number which is chosen to be 0.9. Results are taken at 1.7th second along the tube and given in Figure 12, Figure 13, and Figure 14 while Figure 12 gives variation of density, Figure 13 gives the pressure and, Figure 14 gives the velocity distributions.

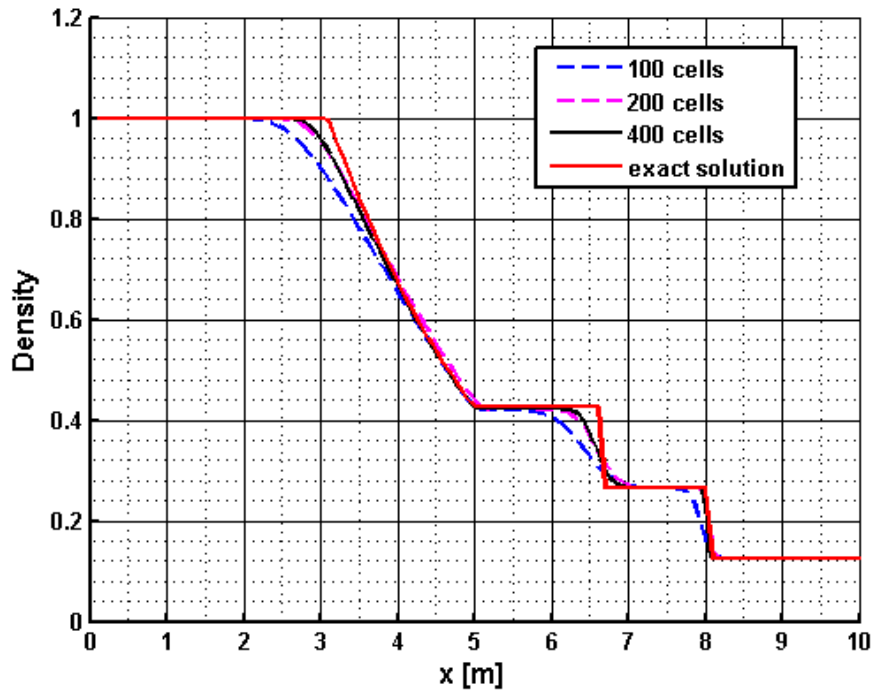


Figure 12: Density distribution at $t=1.7$.

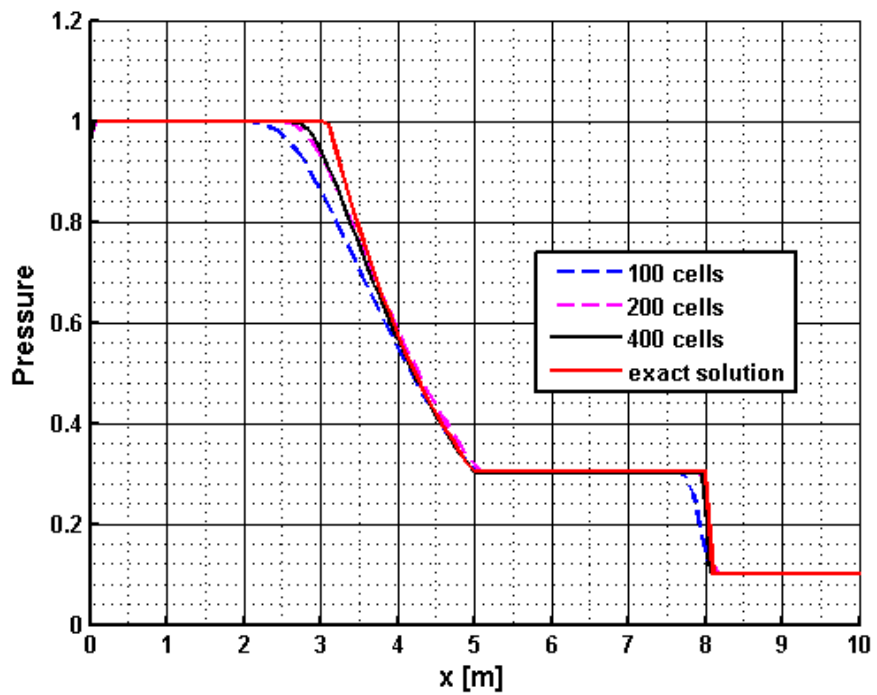


Figure 13: Pressure distribution at $t=1.7$.

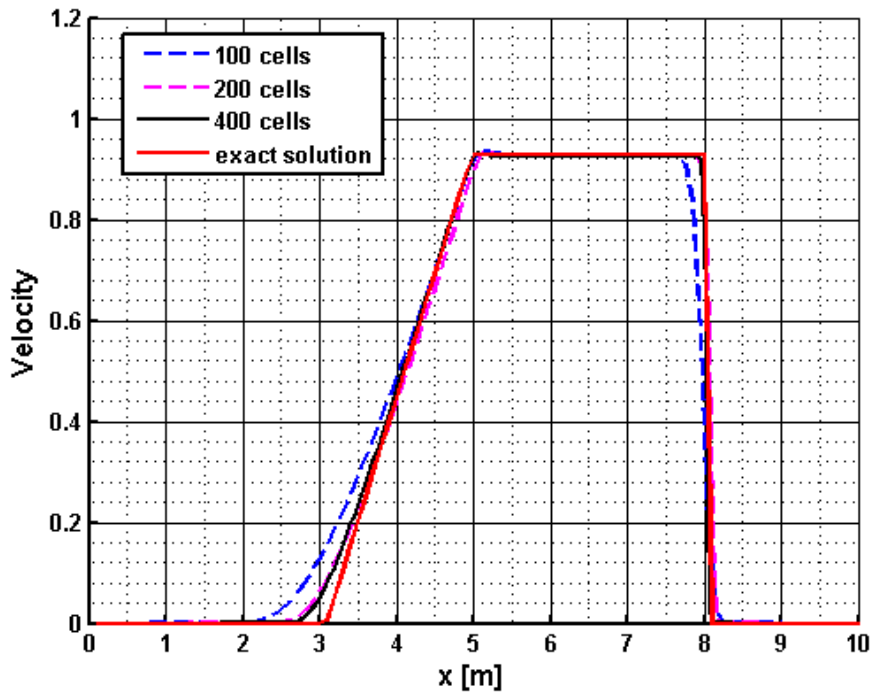


Figure 14: Velocity distribution at $t=1.7$

Breaking the diaphragm starts a process that tends to equalize the pressure in the tube. Gas with higher pressure expands through an expansion wave and flows into lower pressure section. Expansion is a continuous process. Continuously decreasing profile of pressure and density at the left side of the tube, as in Figure 12, and Figure 13, is due to expansion wave. Moreover, at same location, increasing velocity, as in Figure 14, is another characteristic of expansion wave.

As the high pressure gas flows into the right section of the tube, it compresses the low pressure gas. The compression generates a shock wave propagating to the right. Shock wave implies a discontinuity at pressure, density and velocity as seen in Figure 12, Figure 13, and Figure 14.

Point where the density is discontinuous but the velocity and pressure is continuous is called contact discontinuity as seen in Figure 12.

As it can be seen from the Shock tube solutions, density, pressure and velocity distributions are in well agreement with the exact solution. Solutions are smooth, without oscillations. Scheme captures the shock wave accurately and sharply as clearly seen in Figure 13, and Figure 14. However, as in Figure 12, solution is little dissipative around contact discontinuity. Solutions becomes similar to the exact ones as the number of cells increases (i.e. grid size decreases) which is an expected result.

4.2. NOZZLELESS SPRM EXPERIMENTAL CASE

In this section, numerical solutions are carried out for the experimental case of [4]. In their experiments, a nozzleless SPRM with 2 different geometries was considered. The used dimensions for these 2 configurations are given in Table 1. Definitions of these dimensions can be seen in Figure 15.

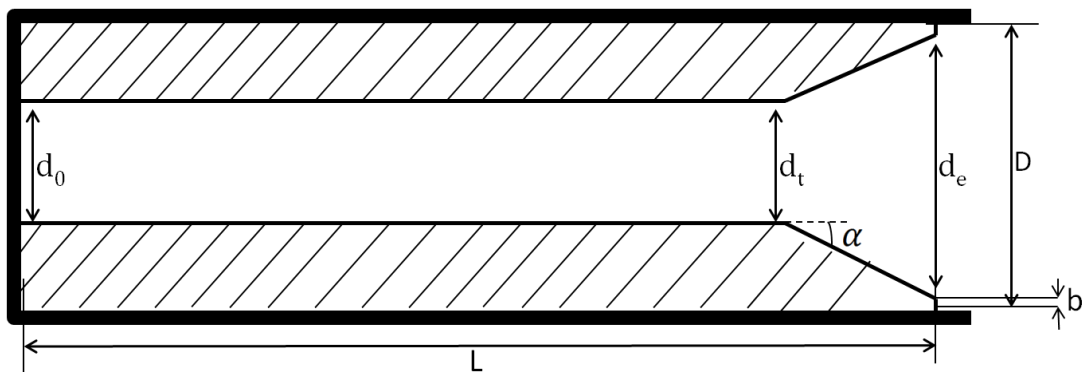


Figure 15: Definitions of dimensions of nozzleless SPRM given in [4]

Table 1: Dimensions of test case geometry

Name	L [mm]	d0 [mm]	dt [mm]	de [mm]	b [mm]	L/D	α (deg)
A	408.94	16.4	19.6	36.22	11.1	7	13
B	525.78	15.89	20.11	36.73	10.85	9	13

For both A and B motor configurations, named motor A and motor B, the outer grain diameter is 58.42 mm.

Normal burning rate variation of propellant is defined by Saint Robert's law. They obtained two different relations for two different pressure intervals. Burning rate measurements was done by using ballistic evaluation motors.

$$r_0 = a \left(\frac{p}{p_{ref}} \right)^n$$

Where p_{ref} is taken to be 1 bar and unit of p is bars as well. Between 4.5 and 15.5 bars a and n coefficients are defined as follows:

$$a = 0.005965 \text{ m/s} \quad \text{and} \quad n = 0.305$$

Between 15.5 and 43 bars, normal burning rate coefficients are defined as follows:

$$a = 0.002849 \text{ m/s} \quad \text{and} \quad n = 0.57$$

For these values of a and n , the burning rate is plotted in Figure 16.

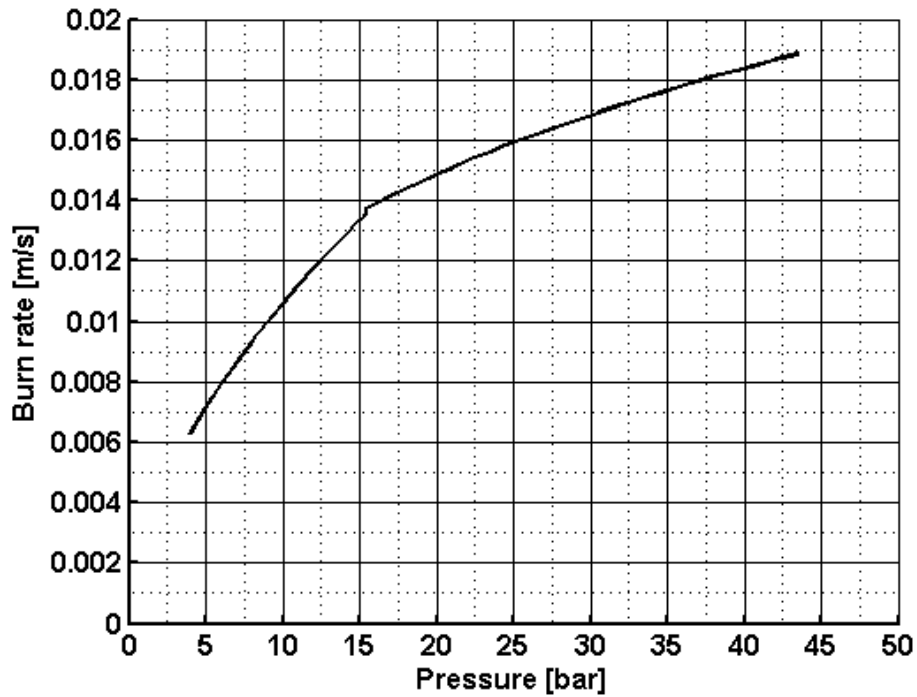


Figure 16: Variation of Burn rate with pressure for the propellant given in [4]

Chemical and transport properties of combustion gases (specific heat ratio, total enthalpy, gas constant and viscosity) are taken from the NASA CEA [44] software. As an input to the software, chemical composition of the propellant is provided.

Simulations are carried out for the A and B motors that the geometric dimensions defined in this section and the results are compared with the experimental results given in [4]. Grid and time step sensitivity analyses are conducted using Motor B configuration. Simulations are done for both unsteady and quasi-steady approach.

4.3. GRID RESOLUTION AND TIME STEP SENSITIVITY

In order to examine the effect of grid resolution and time step size on the results, sensitivity analyses are carried out with quasi steady solutions of Motor B defined in section 4.2. Two sets of results are presented. First one is done with constant grid

resolutions for different times step sizes. Second one is done with constant times step sizes for different grid resolutions.

Grid resolution sensitivity analyses are performed for three different grid resolutions with $\Delta x = 0.01 \text{ m}$, $\Delta x = 0.005 \text{ m}$ and $\Delta x = 0.001 \text{ m}$ for two different time steps with $\Delta t = 0.1 \text{ s}$ and $\Delta t = 0.01 \text{ s}$ to see the effect of time step size on grid sensitivity. Pressure time and thrust time histories with $\Delta t = 0.1 \text{ s}$ are given in Figure 17 and Figure 18, and with $\Delta t = 0.01 \text{ s}$ are given in Figure 19 and Figure 20, respectively.

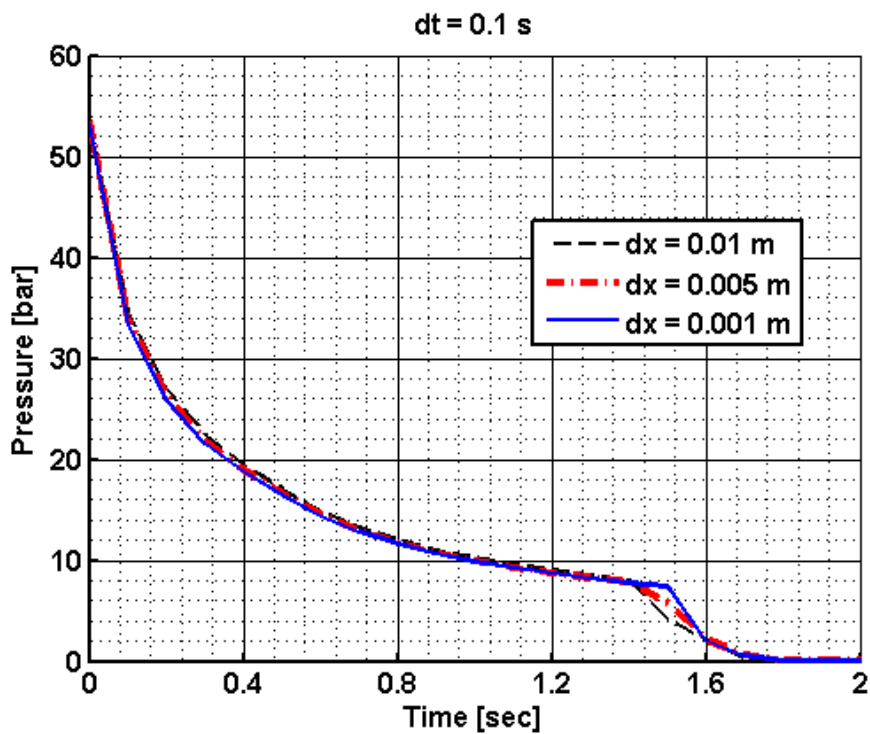


Figure 17: Pressure-time profiles for different grid lengths with 0.1 s time steps.

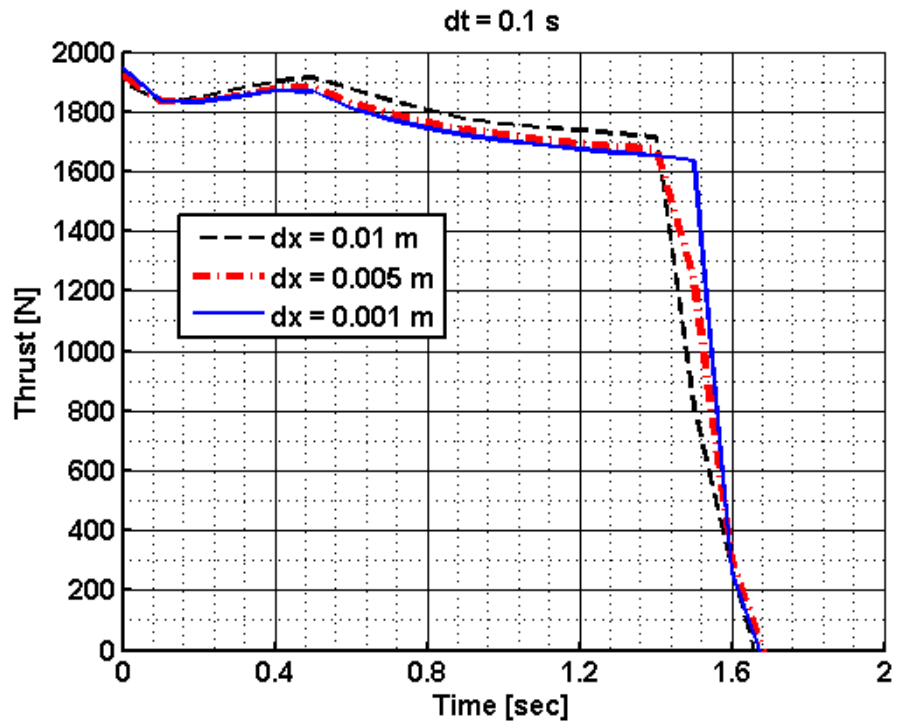


Figure 18: Thrust-time profiles for different grid lengths with 0.1 s time steps.

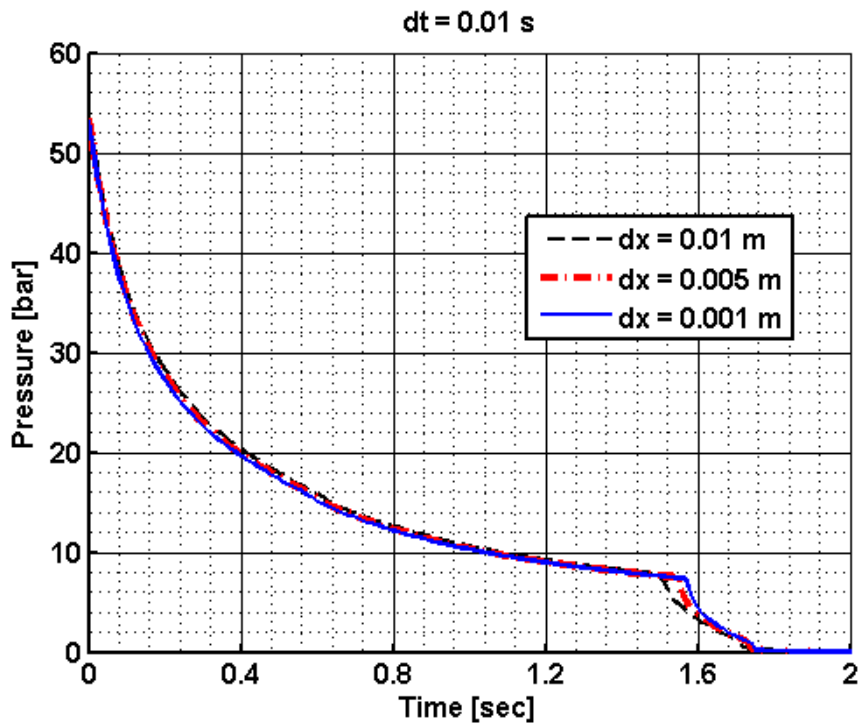


Figure 19: Pressure-time profiles for different grid lengths with 0.01 s time steps.

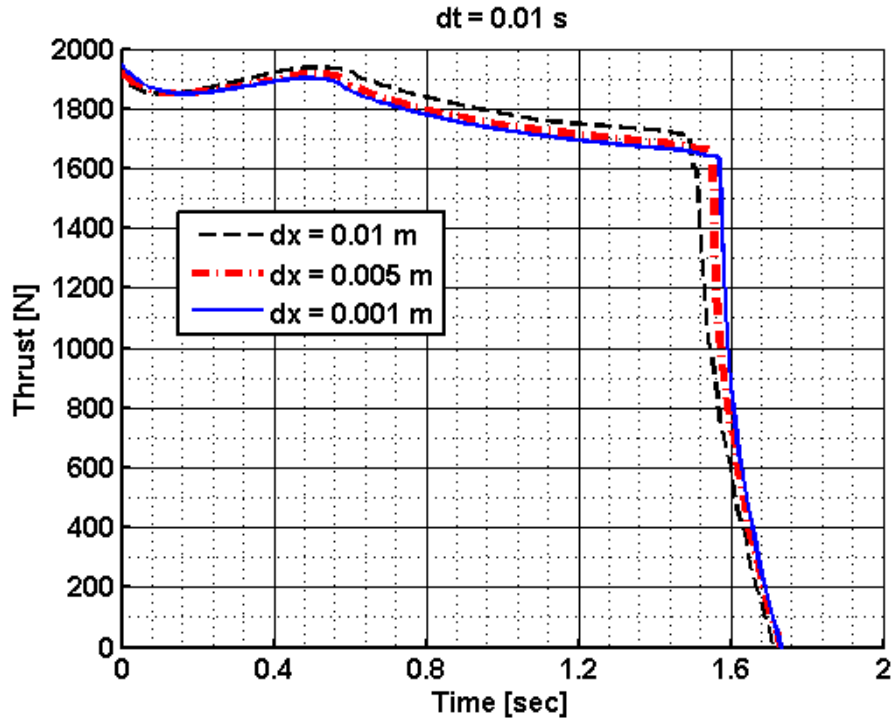


Figure 20: Thrust-time profiles for different grid lengths with 0.01 s time steps

As it can be seen in Figure 17 and Figure 19, effects of grid resolution on predicted pressure time profiles are small. One important effect is on the burning time of the motor till the tail-off starts, as it can be seen on both pressure and thrust-time profiles. When profiles are examined, it is observed that initial thrust values for smaller grid sizes are slightly higher than the predictions with larger grid sizes. Effect of grid resolution on results is very similar for $\Delta t = 0.1 s$ and $\Delta t = 0.01 s$. It can be concluded that, the time step size is not majorly influential on grid resolution sensitivity.

Time step size sensitivity is carried out for two different time steps with $\Delta t = 0.1 s$ and $\Delta t = 0.01 s$ for two different grid lengths $\Delta x = 0.01 m$ and $\Delta x = 0.001 m$. Pressure time and thrust time histories with $\Delta x = 0.01 m$ grid lengths are given in Figure 21, Figure 22 and with $\Delta x = 0.001 m$ grid lengths are given in Figure 23 and Figure 24, respectively.

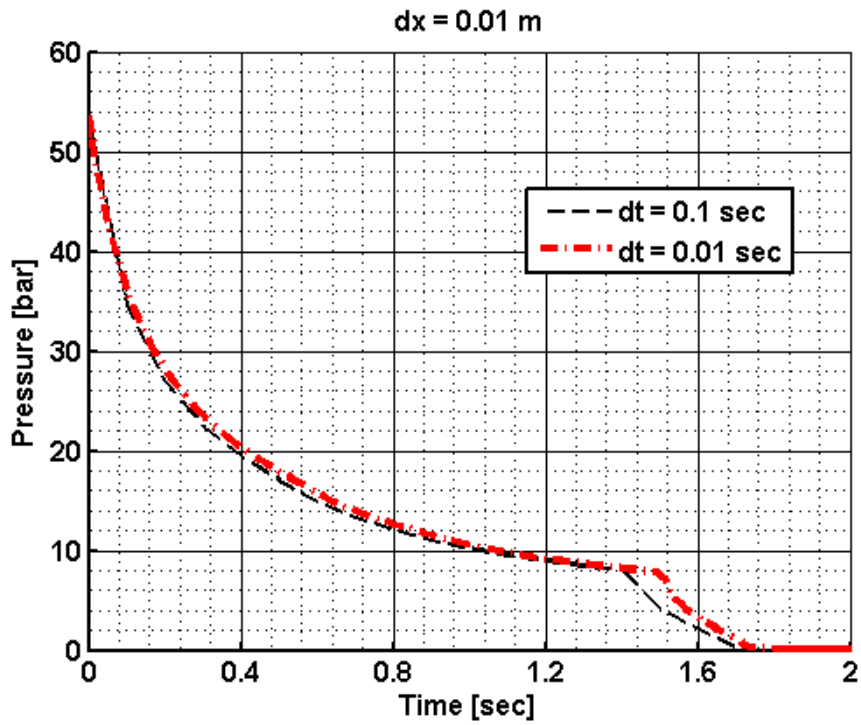


Figure 21: Pressure-time profiles for different time steps with 0.01 m grid length

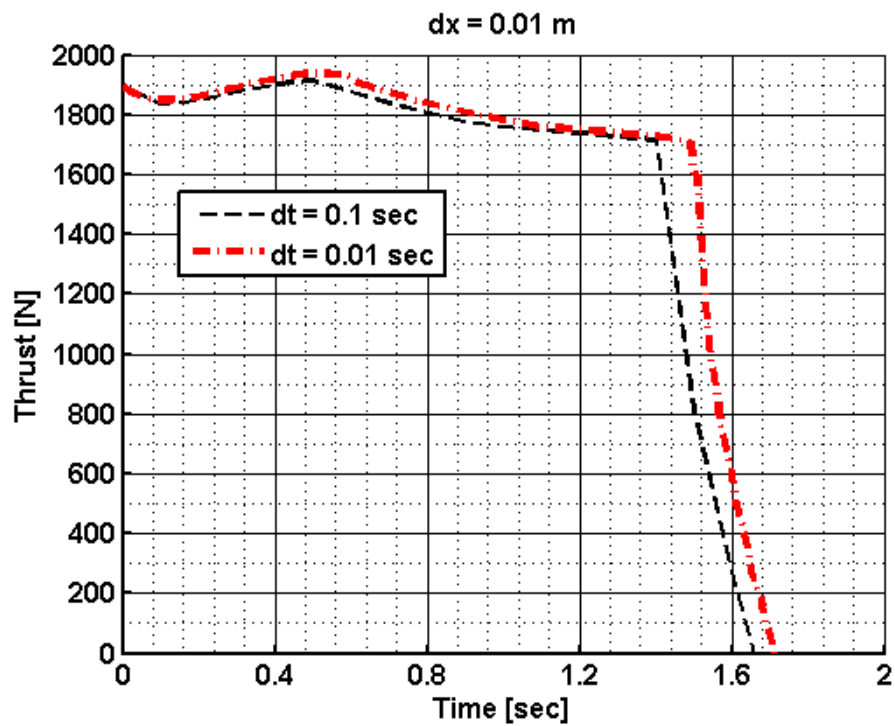


Figure 22: Thrust-time profiles for different time steps with 0.01 m grid length

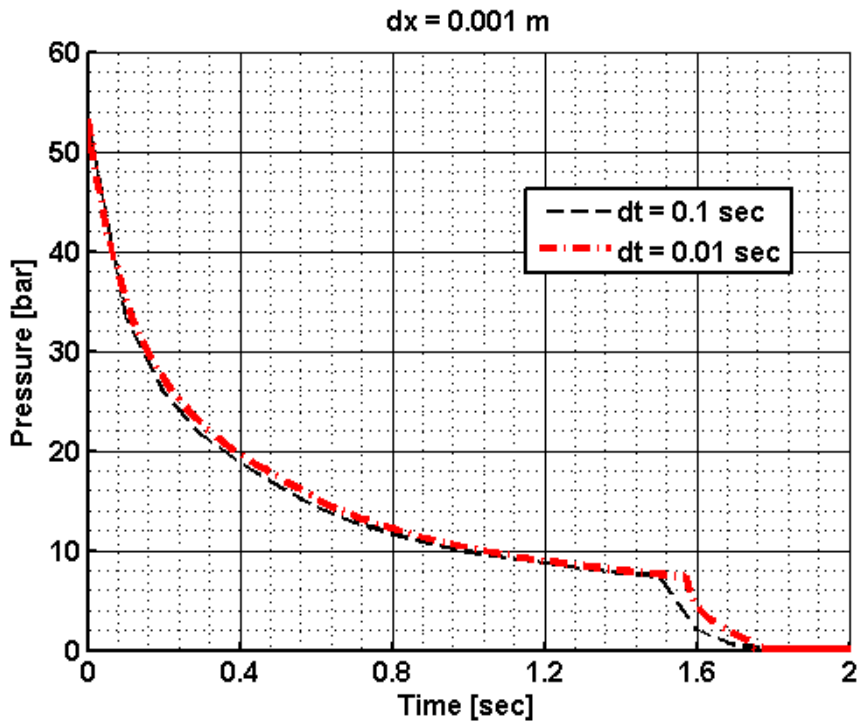


Figure 23: Pressure-time profiles for different time steps with 0.001 m grid length.

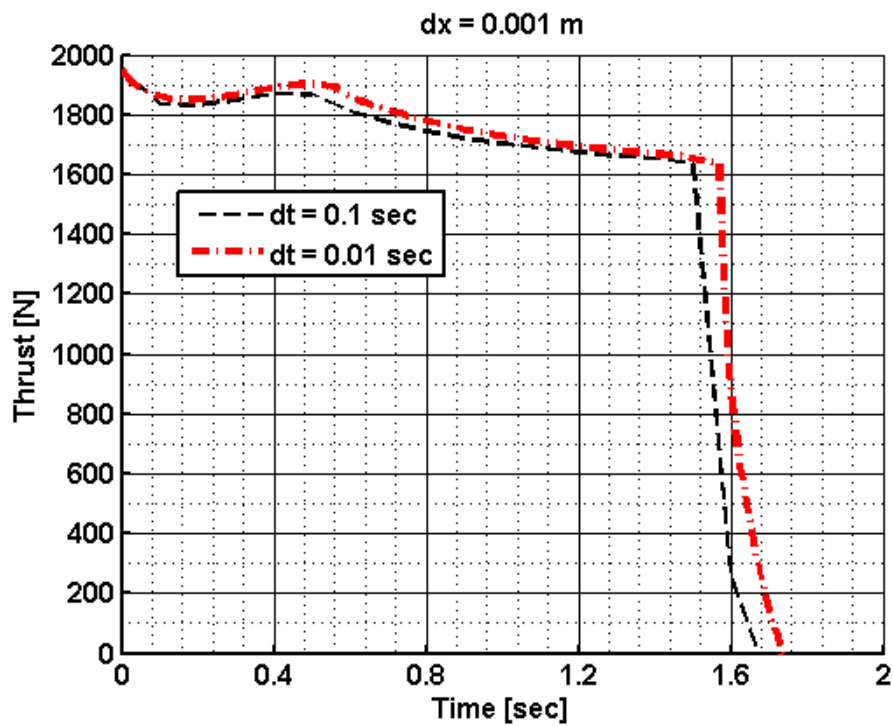


Figure 24: Thrust-time profiles for different time steps with 0.001 m grid length.

As it can be seen on Figure 21 - Figure 24, for smaller time step sizes, burning duration before tail off is higher. With smaller time step sizes, burnback distance for each time step is smaller as well. Therefore, smaller time step size allows calculating burnback steps in a more accurate manner just before the grain burning surface reaches to the case. For smaller time step size, both the thrust and pressure time traces are slightly higher than the results of higher time step predictions. Effect of time step size on results is very similar for $\Delta x = 0.01 \text{ m}$ and $\Delta x = 0.001 \text{ m}$. It can be concluded that, the grid resolution is not majorly influential on time step size sensitivity.

4.4. QUASI STEADY SOLUTIONS

In this section comparison between the quasi steady performance predictions of this study and the experimental data presented in [4] are given. Performances of the two motor configurations are predicted and results are compared with respect to head-end pressure and thrust time histories. Head-end pressure and thrust histories for motor A are given in Figure 25 and Figure 26, respectively.

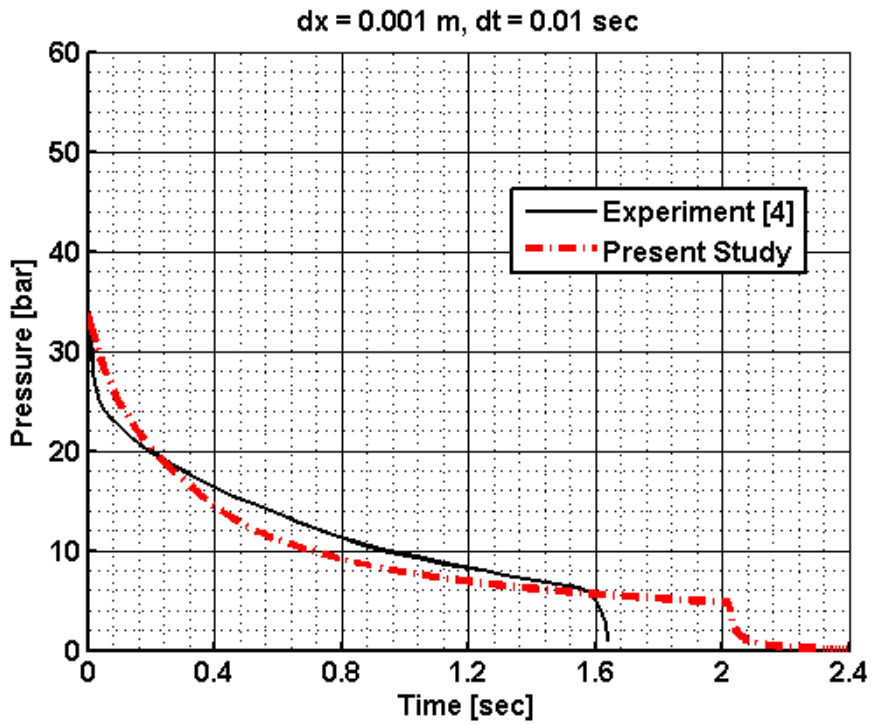


Figure 25: Head end pressure-time profiles of motor A.

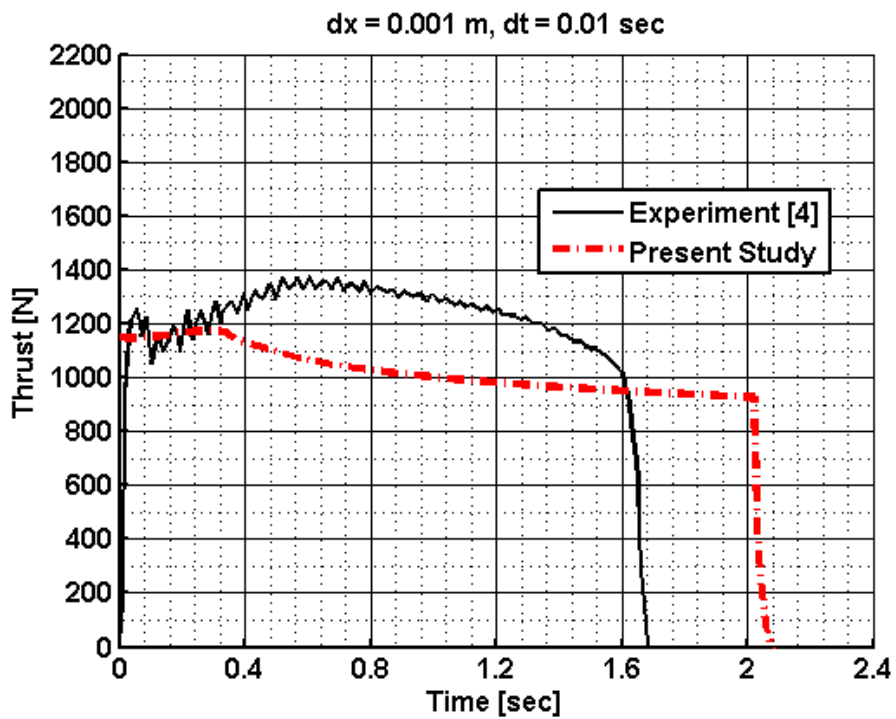


Figure 26: Thrust-time profiles of motor A.

As seen in Figure 25 Initial pressure prediction is nearly same with the experimental value. However, pressure prediction is slightly lower than the actual value after around 0.3 seconds. Moreover it is also the same point where the predicted thrust values starts to move away from the experimental results. Because of the fact that universal erosion model is used, burning rate at the fluid throat may not be exactly predicted and area of fluid throat is one of the major parameters that effects head end pressure considerably, pressure after 0.3 seconds is underpredicted. Underpredicted pressure directly affects the burning rate and thrust. This is the main reason for deviation of predicted thrust curve from the experimental result as given in Figure 26.

If the areas under the thrust-time profiles for motor A are calculated to compare the total impulses, result from the experiment and prediction is found to be respectively, 2029 and 2092 N.s, where the prediction is 3.1% higher. Although the predicted average pressure is slightly lower than the experiment, which drops the specific impulse and total impulse, because to the fact that prediction does not include any losses, it is acceptable to have higher predicted total impulse than the experiment.

On the quasi steady time interval of burning (i.e. time interval which does not include ignition transition and tail-off phases), due to cylindrical shape of the grain, burning area increases. On the other hand, increasing area of the fluid throat results in decreasing head end pressure. For a constant solid propellant density during its operational time, generated mass flow rate is mainly function of burning area and burning rate. Two different burning rate relations of propellant for different pressure intervals are the main reason for increasing and decreasing trend for both experiment and prediction. As the pressure drops, burning rate exponent (n) increases, that makes propellant much more sensible to the pressure change. In this sensible region, under predicted pressure also results in longer predicted operation time of the motor.

Performance of another configuration with same propellant but different grain geometry, is named B motor, is predicted as well. Head-end pressure and thrust histories for motor B are given in Figure 27 and Figure 28.

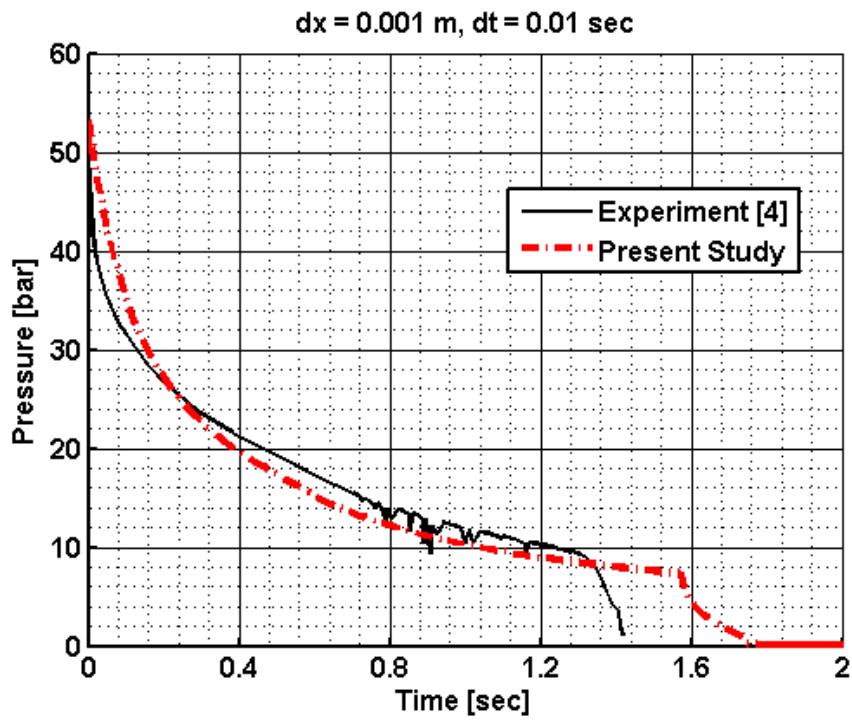


Figure 27: Head end pressure-time profiles of motor B.

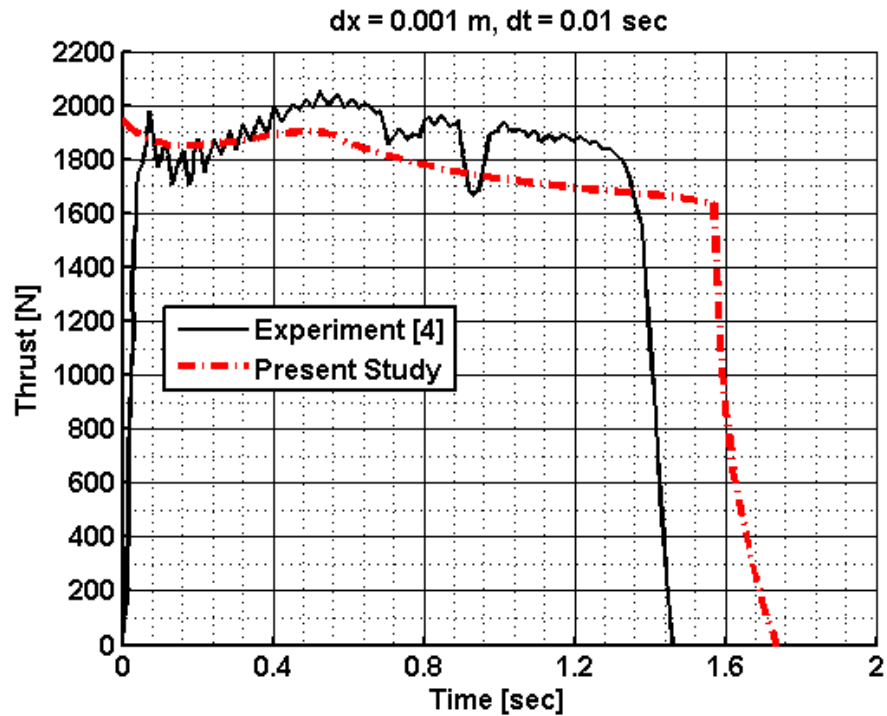


Figure 28: Thrust-time profiles of motor B.

Total impulses, results from the experiment and prediction of motor B are found to be respectively, 2640 and 2890 N.s that the prediction is 9.4% higher. Pressure history prediction of motor B is better than motor A and effect of this is also seen in thrust history. Total impulse deviation is more than motor A because the pressure history is closer to the experimental value, which reveals the amount of losses more clearly. For motor A, due to under prediction of pressure, performance without losses are under predicted as well. For motor B, due to the fact that performance without losses is not as under predicted as in the motor A, total impulse deviation seems to be higher.

Initial pressure prediction is nearly same with the experimental value. As in the motor A, after the predicted pressure curve drops down of the experimental data, thrust profile starts to recede from the experimental data as well.

Erosion mode developed by Mukunda and Paul [1] are not based on data obtained for very low operational pressures (i.e. lower than 10 bars). This may be the main reason for deviation of predicted time histories as the pressure drops.

4.5. UNSTEADY SOLUTIONS

The developed performance prediction code is capable of performing both quasi steady and unsteady analyses. To see the difference between two different approaches, performance of motor B defined in section 4.2 is predicted with 0.001 m grid resolution. For quasi steady analysis time step is taken to be 0.01s, while unsteady solutions is completed with constant time step of 10^{-7} seconds. Initial conditions for unsteady simulations are taken to be, 1 bar for internal pressure of grain port with 300 K and stationary gas inside the rocket motor. For both simulations, exit pressure is taken to be 1 bar.

Head end pressure and thrust histories for both unsteady and quasi steady solutions are given in Figure 29 and Figure 30.

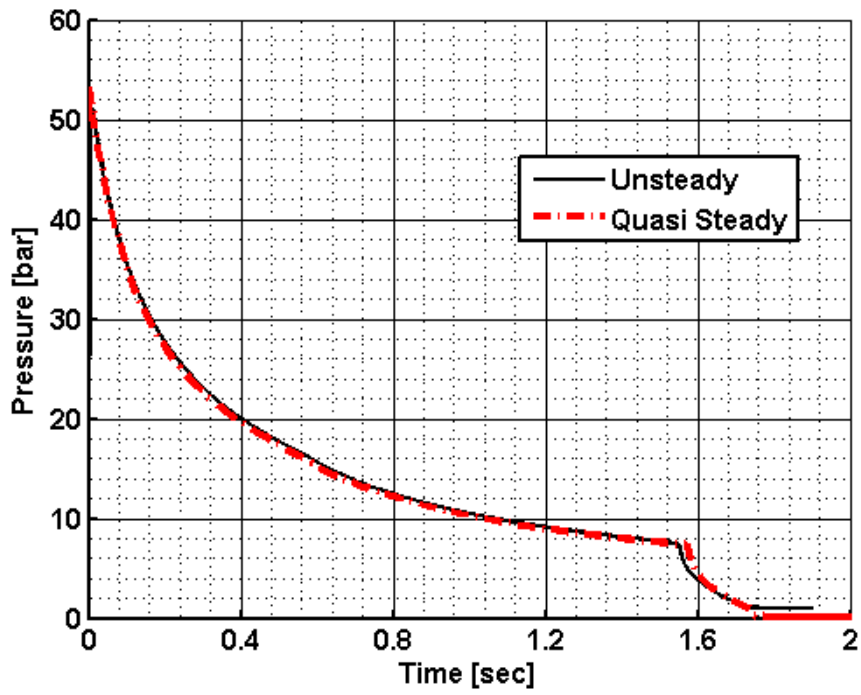


Figure 29: Variation of head end pressure for unsteady and quasi steady approach

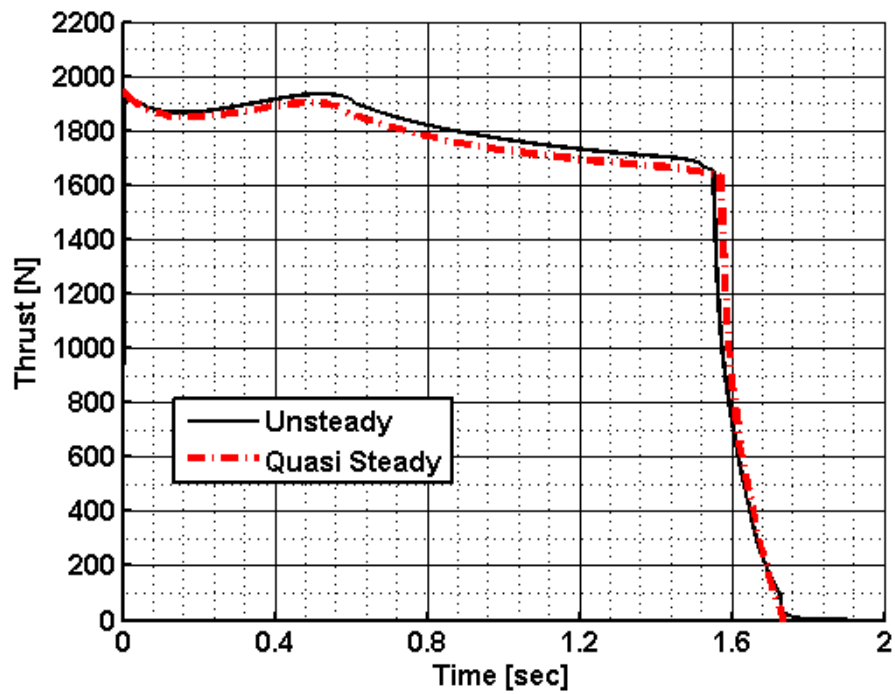


Figure 30: Variation of thrust for unsteady and quasi steady approach

As it can be seen in Figure 29 and Figure 30, during the quasi steady phase of the operation, calculated values are very close to each other. A major difference shows itself on unsteady phases of burning, i.e. ignition transient and tail-off regions. Close up views of Figure 29 and Figure 30 for the first 0.05 seconds of operation are shown in Figure 31 and Figure 32. As evident in the Figure 31 and Figure 32, unsteady approach allows to calculate ignition transient region where the internal cavity, which is 1 bar initially, is filling up.

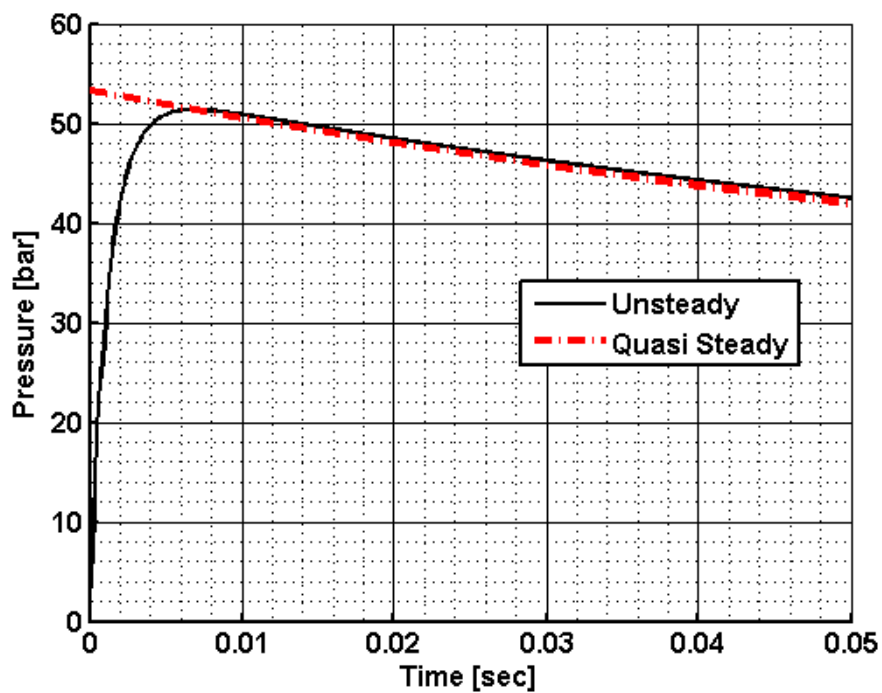


Figure 31: Variation of head end pressure for unsteady and quasi steady approach (close up view of Figure 29)

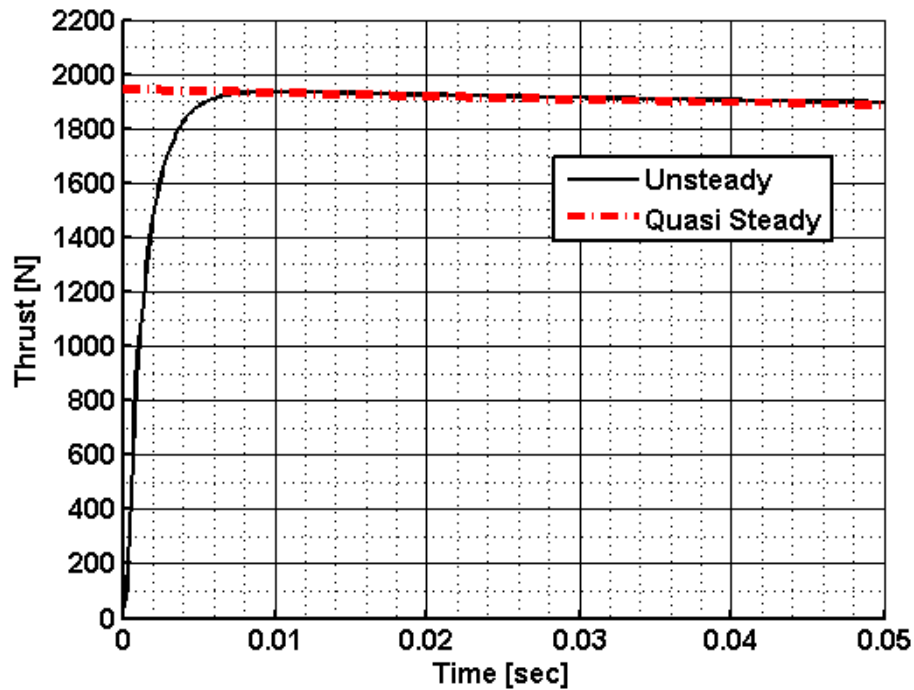


Figure 32: Variation of thrust for unsteady and quasi steady approach (close up view of Figure 30)

4.6. DETAILED EXAMINATION OF TEST CASE PREDICTIONS

In order to examine the flow field inside the grain port and regression characteristics of grain itself, pressures, Mach numbers, burning rates and grain port radii along the grain for different times of operation are observed from quasi steady solutions.

Mach number distribution along the grain gives information related to choking point of flow and the reached value at the motor exit. Mach number distribution for $\Delta x = 0.01 \text{ m}$ and $\Delta x = 0.001 \text{ m}$ are given respectively in Figure 33 and Figure 34.

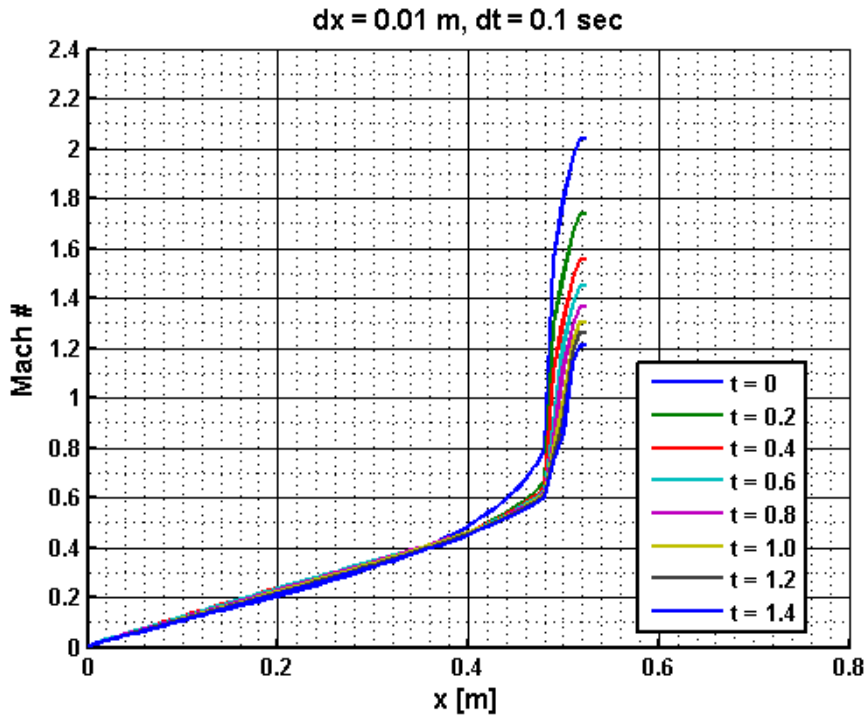


Figure 33: Mach number distribution along the port for 0.01 m grid length.

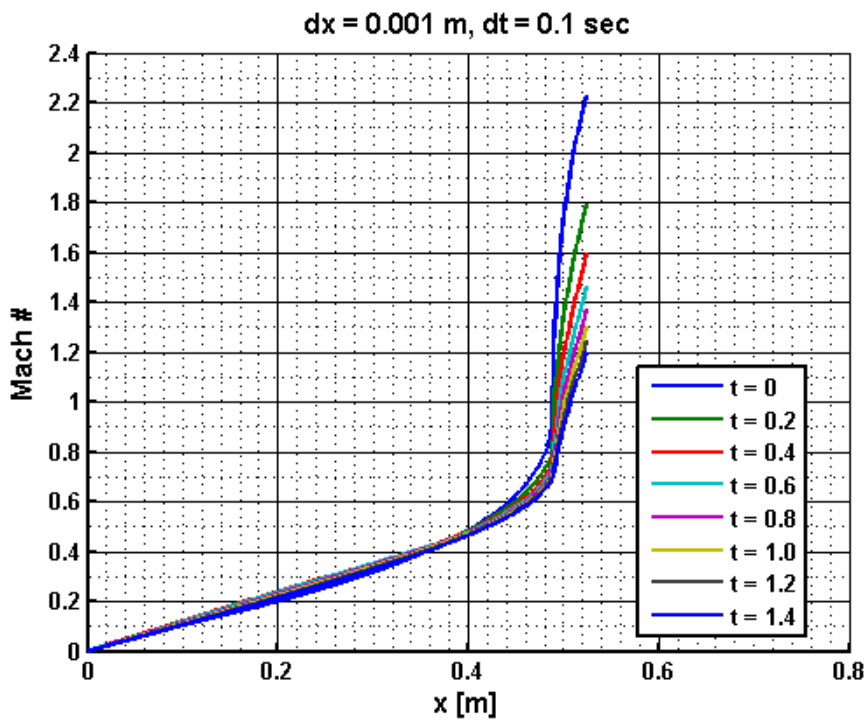


Figure 34: Mach number distribution along the port for 0.001 m grid length.

As evident from Figure 33 and Figure 34 that Mach number distributions along the grain port do not change significantly with time except in the exit cone, where due to uneven burning rate of the grain, exit cone geometry changes with time, which is shown in Figure 35 and Figure 36. Results for $\Delta x = 0.01 \text{ m}$ and $\Delta x = 0.001 \text{ m}$ are quite similar but exit Mach number is slightly higher according to analysis done with $\Delta x = 0.001 \text{ m}$.

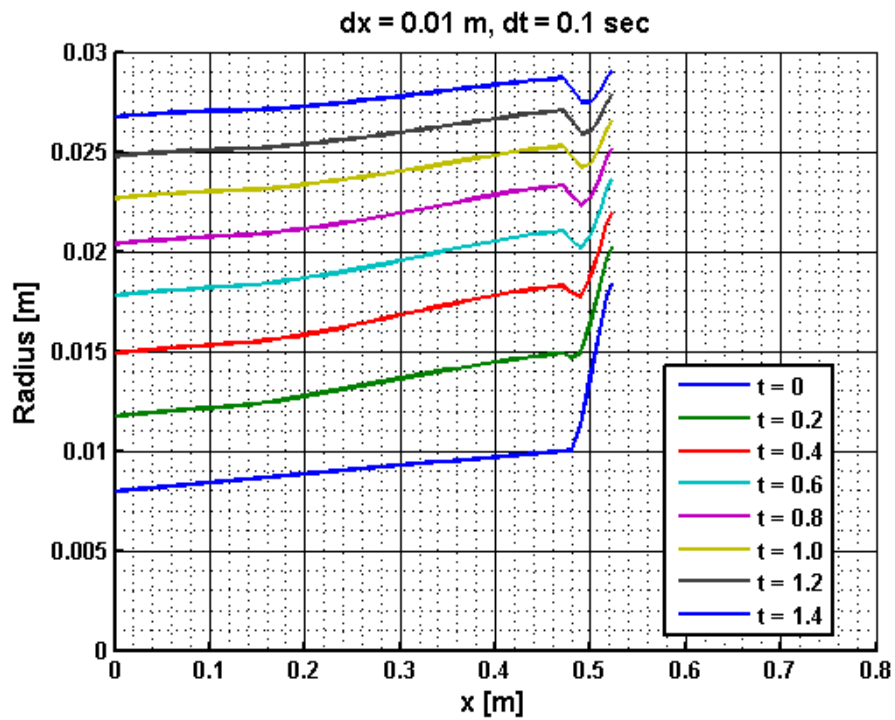


Figure 35: Port radius distribution along the grain for 0.01 m grid length.

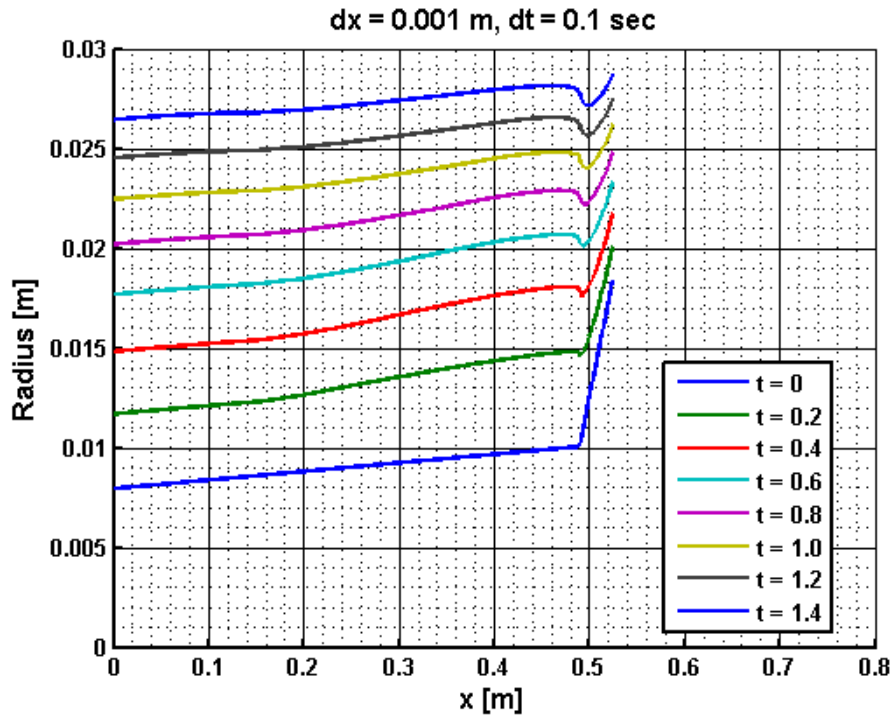


Figure 36: Port radius variation along the grain for 0.001 m grid length.

On Figure 35 and Figure 36, burnback of grain is seen clearly. Slope of exit cone decreases as the time increases which results in the fact of having decreasing exit Mach number. This severe change of slope of exit cone implies that the burning rate at the beginning and exit of the cone are considerably different. Moreover, grain shape evolution is directly related to local burning rates along the grain. Therefore, to have an idea on the reasons for this type of grain shape evolution, burning rates along the grain, given in Figure 37 and Figure 38 are studied.

There are two mechanism included in the calculation of burning rate defined in Section 3.2. These are the normal burning rate r_0 , which depends on local pressures only, and the erosive burning rate, which is function of several flow properties but mainly local mass flux. According to erosion model [20] used in this study, there is a threshold value up to which the erosive burning is assumed to be zero. This is the main reason for the observed burn rate curves given in Figure 37 and Figure 38. Moreover, on the

exit cone, although the cross flow velocity is considerably high, burn rate is relatively low. To understand the reasons behind these phenomenons, both the normal burning rate and erosive burning rate contribution along the grain is examined in Figure 39 and Figure 40.

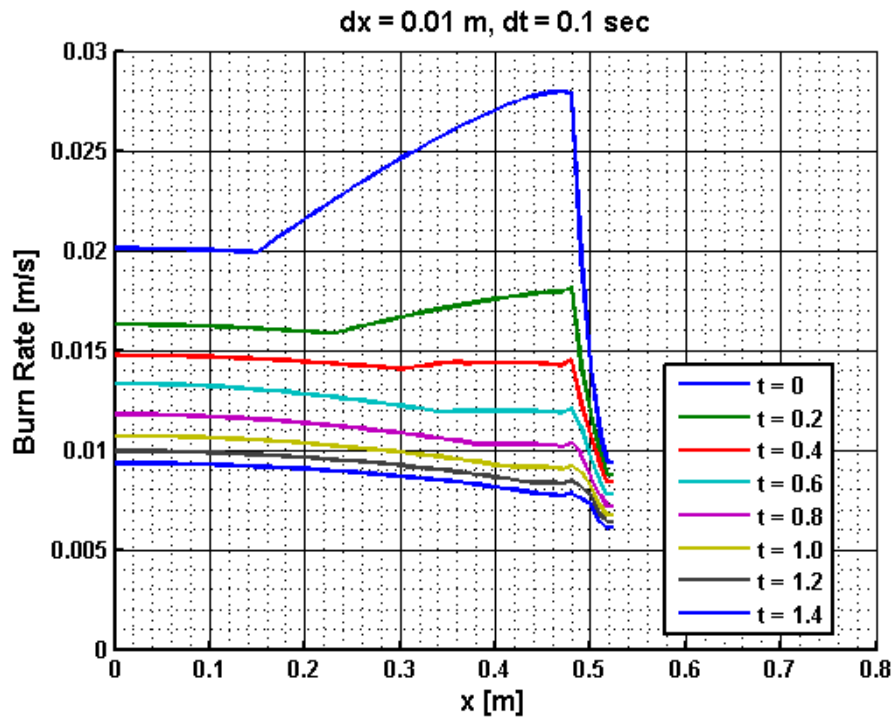


Figure 37: Variation of burn rate along the grain for 0.01 m grid length.

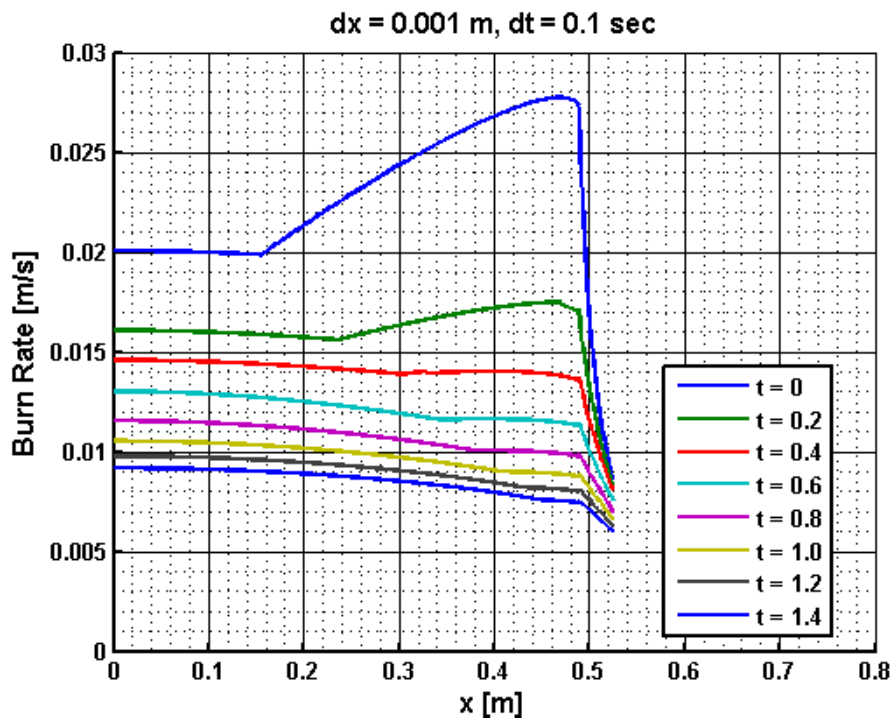


Figure 38: Variation of burn rate along the grain for 0.001 m grid length.

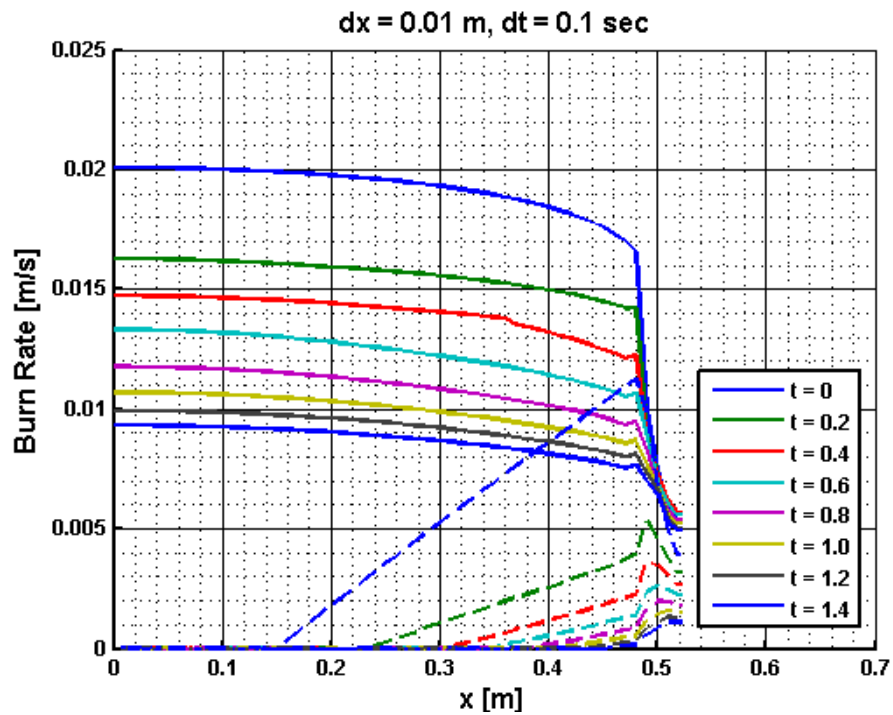


Figure 39: Normal (solid lines) and erosive (dashed lines) burn rate along the grain for 0.01 m grid length

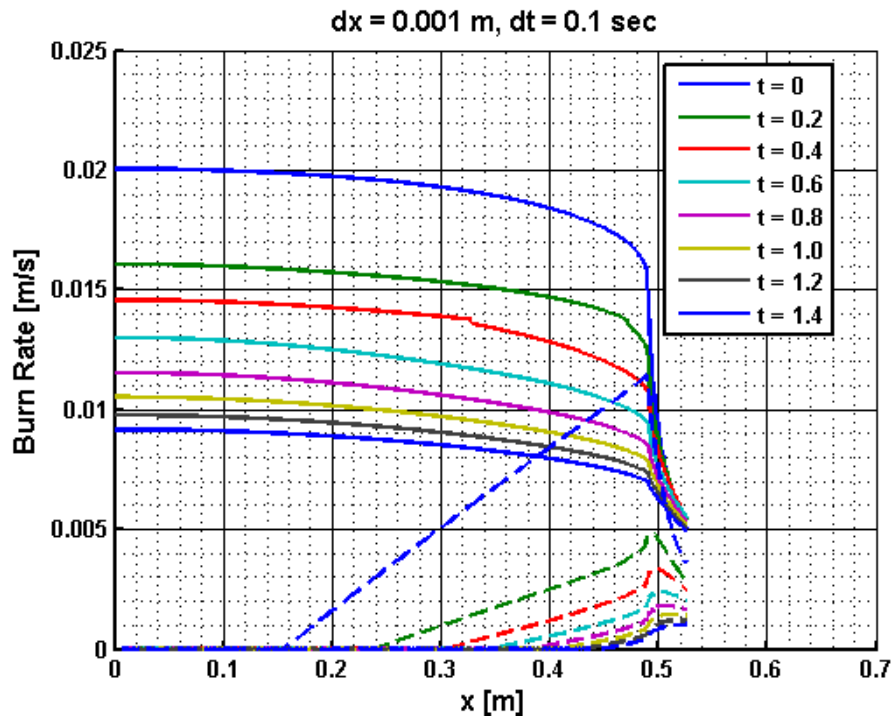


Figure 40: Normal (solid lines) and erosive (dashed lines) burn rate along the grain for 0.001 m grid length

Along the grain due to decreasing static pressure, normal burning rate decreases. On the other hand, increasing fluid velocity, increases the erosive burning. Maximum burning rate is obtained near the choking point of flow. Due to expansion up to supersonic speeds, pressure drops rapidly on the exit cone. Furthermore, erosive burning effect starts to decrease due to decreasing mass flux. As a result, relatively low burning rate is obtained close to the exit of nozzleless grain.

CHAPTER 5

PARAMETRIC STUDIES

In this section some parametric studies are discussed. Specifically, effect of exit cone and burning rate pressure exponent are examined. 3 different fictitious motor configurations are considered. Analyses are conducted with $\Delta x = 0.001 \text{ m}$ and $\Delta t = 0.1 \text{ m}$ using quasi steady method. Specifications of the considered configurations are summarized in Table 2.

Table 2: Specification of motor configurations.

Configuration ID	X	Y	Z
Diameter	3D	3D	3D
a coefficient [mm]	0.01238	0.01238	0.004
n coefficient	0.23	0.23	0.50
Normal burn rate at 70 bars [mm]	32.89	32.89	33.47
Non-dimensional Propellant Volume	99.05	100	99.05
Exit Cone	Yes	No	Yes

Grain geometry for the X and Z configuration is given in Figure 41. Grain geometry of configuration Y is almost same but the only difference is that port area is constant along the grain. In other words, there is not exit cone.

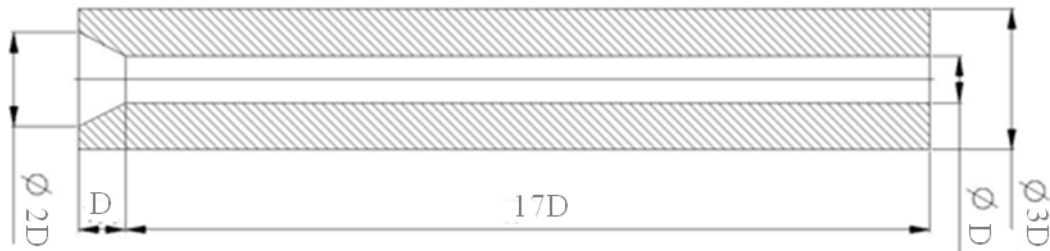


Figure 41: Grain geometry for motor configurations X and Z.

5.1. RESULTS

5.1.1. Motor X

Head end pressure and thrust variation of Motor X with time are given in Figure 42 and Figure 43, respectively. These figures indicate that, head end pressure decreases with time, in the mean time thrust increases. As the propellant burns, burn area increases but pressure decreases due to the fact that fluid throat area increases. Because of the fact that propellant normal burning rate pressure exponent is relatively low, increasing burn area is dominant than the decreasing burn rate in terms generated combustion gas mass.

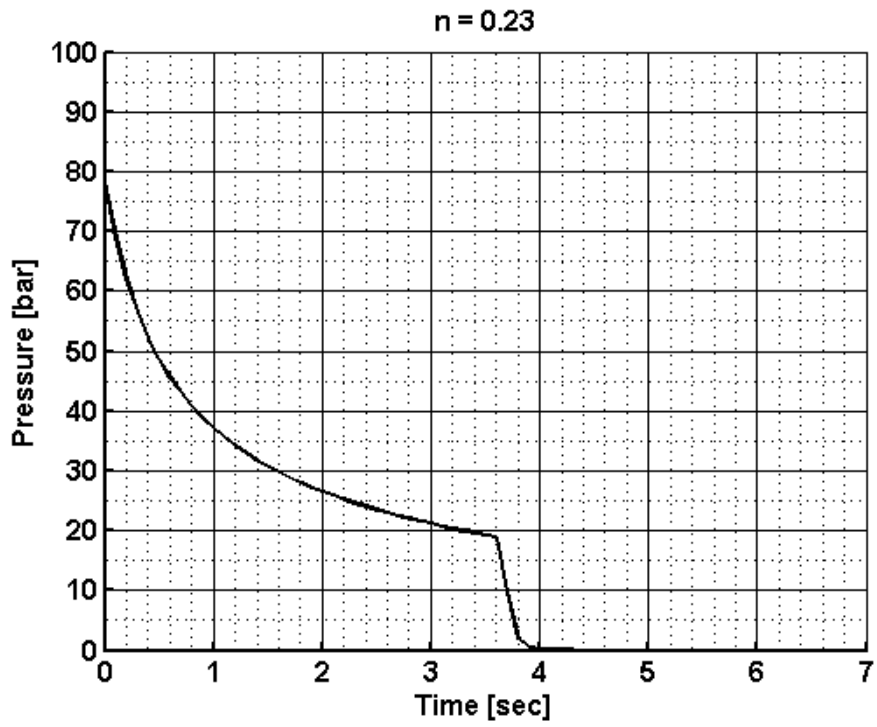


Figure 42: Variation of Head end pressure with time of Motor X

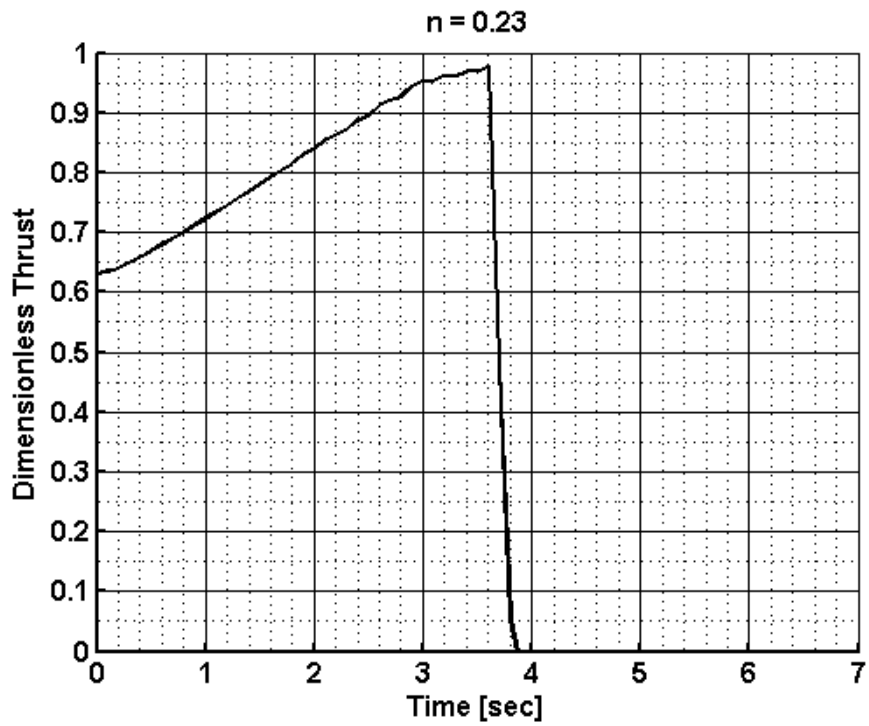


Figure 43: Variation of Dimensionless Thrust with time of Motor X

Motor exit pressure-time curve is given in Figure 44. As it can be seen, exit pressure increases with time during quasi-steady operation. Although the head pressure drops, in Figure 45 it is seen that the expansion ratio of exit cone decreases, that drops the exit Mach number. Moreover, web thickness at the exit of grain is thinner than the other parts of the grain. In other words, grain exit radius reaches to the outer diameter of the grain sooner. After this time, fluid throat area maintains its growing trend but the exit area stays constant and this fact changes the decreasing trend of expansion ratio. This is the main reason of the diffraction of the curve after 3rd second given in Figure 44 and Figure 45.

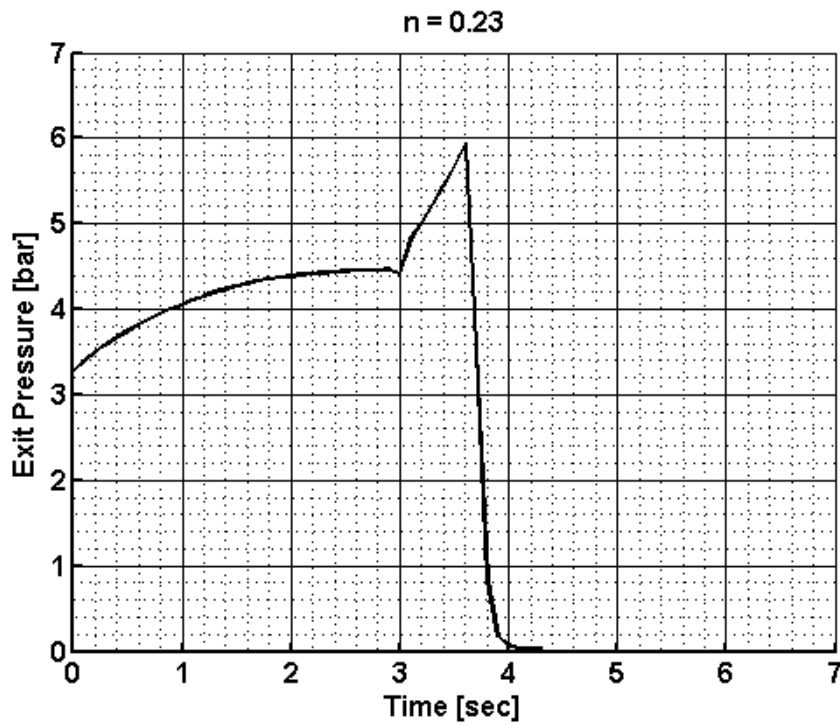


Figure 44: Variation of Exit Pressure with time of Motor X

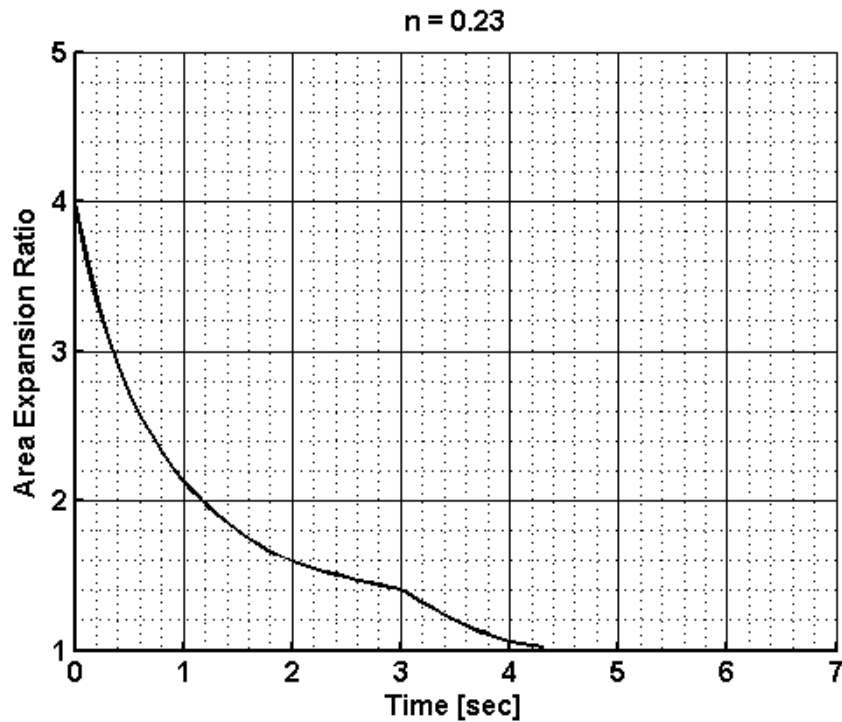


Figure 45: Variation of Area Expansion Ratio of exit cone with time of Motor X.

5.1.2. Motor Y

Motor Y is basically have same properties with Motor X. The difference is that the motor Y does not have exit cone and initial port area is same along the motor axis.

Motor Y head end pressure decreases with time, while thrust increases. As the propellant burns, burn area increases but pressure decreases due to the fact that fluid throat area increases. Because of the fact that propellant normal burning rate pressure exponent is relatively low, increasing burn area is dominant than the decreasing burn rate in terms generated combustion gas mass. Variation of head pressure and dimensionless thrust with time are given in Figure 46 and Figure 47.

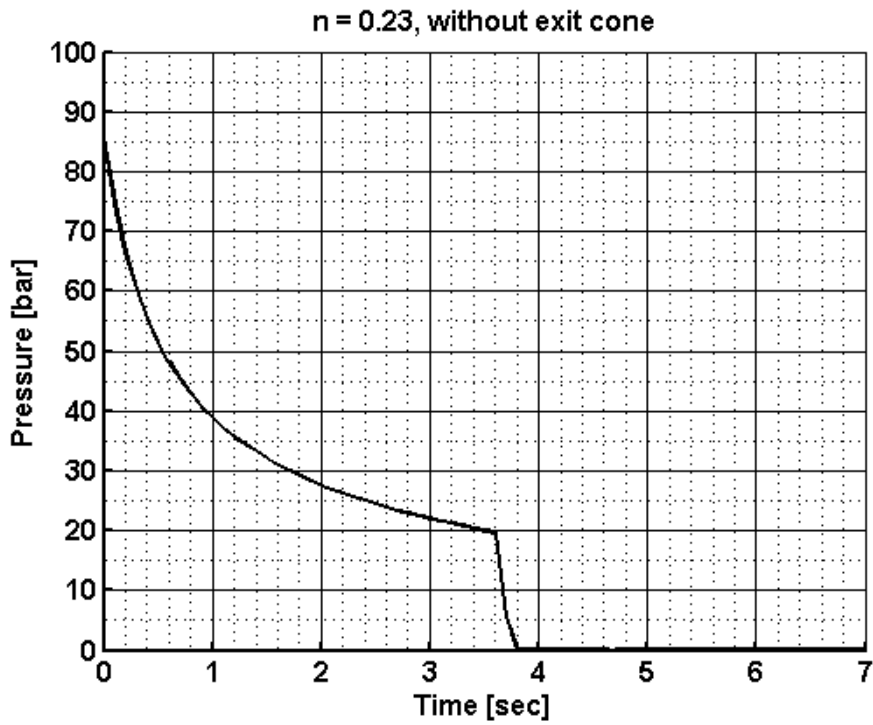


Figure 46: Variation of Head end pressure with time of Motor Y.

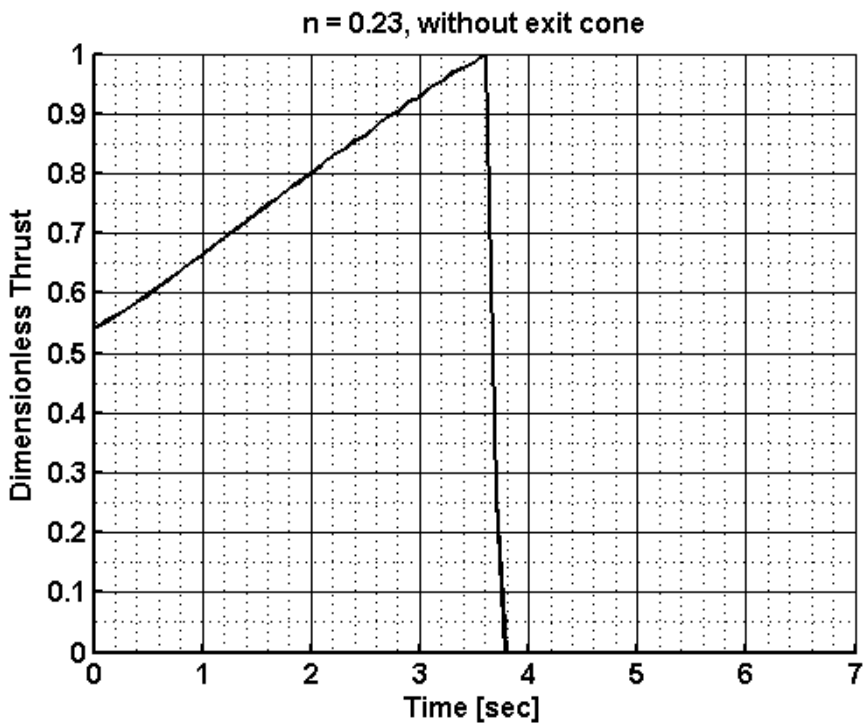


Figure 47: Variation of Dimensionless Thrust with time of Motor Y

As it can be seen on motor exit pressure-time curve, given in Figure 48, exit pressure increases with time during quasi-steady operation. Because there is not exit cone, exit pressure follows the same trend with the head end pressure and exit is always the choking location for the quasi-steady phase of operation.

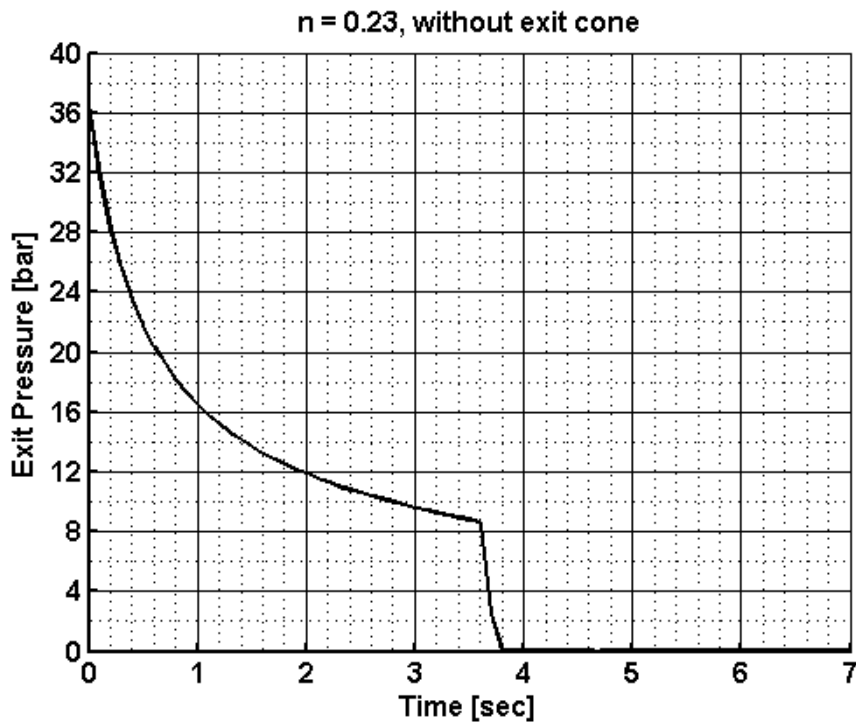


Figure 48: Variation of exit pressure with time of Motor Y

5.1.3. Motor Z

Motor Z has the same geometry with the motor X. However, normal burning rate pressure exponent (n) is different.

Head end pressure history trend of Motor Z, given in Figure 49, is very similar with the Motor X and Motor Y due to mentioned reasons in related sections. However,

although the geometry is same, thrust-time profile given in Figure 50, is considerably different.

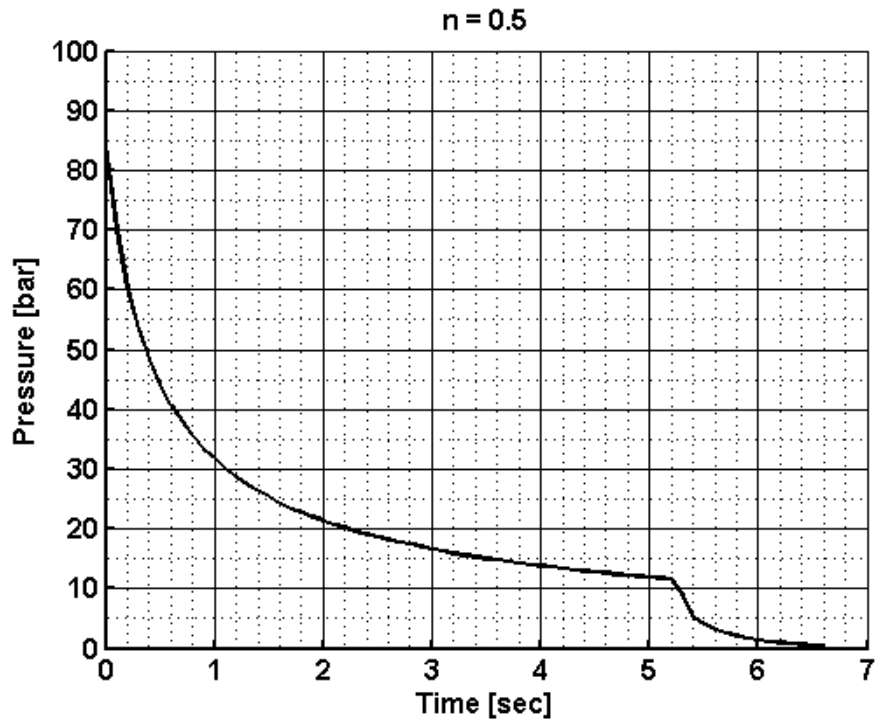


Figure 49: Variation of head-end pressure with time of Motor Z.

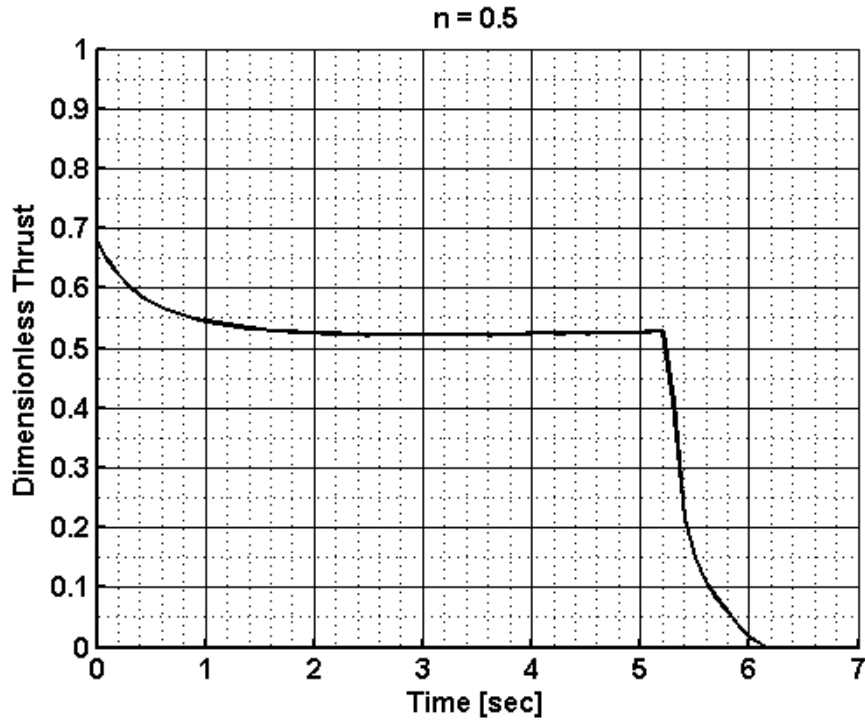


Figure 50: Variation of Dimensionless Thrust with time of Motor Z.

5.1.4. Performance Comparison

In order to see the performance difference of different configurations clearly, thrust history of Motor X, Y and Z are given in Figure 51. As it can be seen, as the propellant normal burning rate increases, increasing burn area becomes comparable with the decreasing burn rate in terms generated combustion gas mass and thrust related to it. In other words, propellant normal burning rate pressure exponent is highly effective on thrust profile of motor and with same grain geometry; although the operating pressures and initial thrust values are close, different thrust time histories can be obtained.

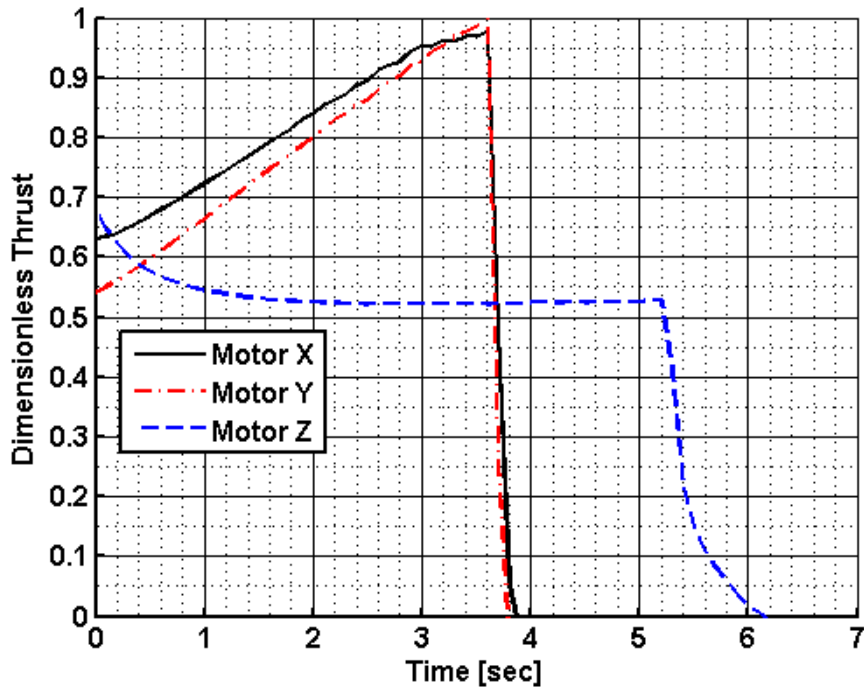


Figure 51: Variation of Dimensionless Thrust with time of Motor X, Y and Z.

Non-dimensional total impulses and average specific impulses are given in Table 3 where the total impulses and average specific impulses are calculated up to time when the exit pressure of the motor is equal to the 1 bar.

Table 3: Performance comparison of different configurations

Configuration ID	X	Y	Z
Non-dimensional Total Impulse	100	94.33	96.36
Average Isp [s]	201.0	184.6	196.9

In Table 3 it is seen that maximum total impulse is obtained with motor X. Therefore, it can be concluded that the having an exit cone and low normal burning rate pressure exponent n . Although the configuration without exit cone allows to load more

propellant inside the motor, absence of exit cone results in a much more performance deficit which cannot be compensated by the extra amount of propellant.

CHAPTER 6

CONCLUSION AND FUTURE WORK

The purpose of this study was to develop an internal ballistics computer program to predict performance of Nozzleless Solid Propellant Rocket Motors for use in design and development of Nozzleless SPRM.

Flowfield has been modeled as quasi one-dimensional flow with mass addition. To validate the program, first shock tube problem solutions, were presented. Results of shock tube problem show that the used scheme is capable of capturing the shock and contact discontinuities. Secondly, validation against experimental case [4] was given. It is seen that results are promising in terms of predicting thrust and pressure history of a given nozzleless SPRM. Internal flow field and grain regression characteristics of validation cases were examined. It is observed that erosive burning is important in terms of predicting performance of nozzleless motor.

Parametric studies have been conducted to see the effect of different design parameter on overall performance of motor, specifically exit cone and normal burning rate pressure exponent n . It has been observed that the exit cone increases the overall performance of a nozzleless motor significantly and pressure exponent n is highly effective on thrust profile of motor for a same propellant grain geometry.

Developed computer program is capable of predicting the nozzleless solid propellant rocket motor performance in a short time and provides data to be used during the preliminary design by the motor designer.

Possible future areas of interest as future work can be summarized as:

- a) Implementation of different erosion models into the computer program to see the variation of the results for different models.
- b) Implementation of igniter and flame spreading models to simulate the ignition transient phase accurately.

REFERENCES

- [1] G. Kurth and H.-L. Besser, “European Air Dominance Missile Powered by High Energy Throttleable Ducted Rocket.”
- [2] K. J. Fruge, “Design and Testing of a Caseless Solid-Fuel Integral-Rocket Ramjet Engine for Use in Small Tactical Missiles,” 1991.
- [3] I. M. Procinsky and C. a. McHale, “Nozzleless Boosters for Integral-Rocket-Ramjet Missile Systems,” *J. Spacecr. Rockets*, vol. 18, no. 3, pp. 193–199, 1981.
- [4] S. Krishnan and R. Ramakrishnan, “Effect of motor length and propellant formulation on nozzleless solid rocket performance,” *Proc. Inst. Mech. Eng. Part G J. Aerosp. Eng.*, vol. 213, no. 1, pp. 35–44, 1999.
- [5] D. P. Harry, “Status of Nozzleless Solid Rocket Motor Internal Ballistics Analysis,” in *AIAA/SAE 13th Propulsion Conference*, 1977, pp. 1–4.
- [6] J. John, V. Ravikumar, S. Padmanabhan, and K. Selvakumar, “Conceptual Studies on Nozzleless Propulsion,” in *ICMABE’2012*, 2012.
- [7] R. Farinaccio and P. Lessard, “Nozzleless Booster Performance Study,” 2002.
- [8] G. Alon and I. Aharon, “Internal Ballistics Considerations of Nozzleless Rocket Motors,” *J. Propuls. Power*, vol. 15, no. 6, pp. 866–873, 1999.
- [9] V. R. S. Kumar, B. N. Raghunandan, and T. Kawakami, “Studies on Internal Ballistics of Dual-thrust Motors for Nozzleless Propulsion,” 2010, no. July, pp. 1–10.
- [10] L. D’Agostino, L. Biagioni, and G. Lamberti, “An Ignition Transient Model For Solid Propellant Rocket Motors,” in *37th AIAA Joint Propulsion Conference*, 2001.
- [11] M. Andrenucci, “Unsteady Ballistic Code for Performance Prediction of Solid Propellant Rocket Engines,” *AIAA*, no. July, pp. 1–9, 2007.

- [12] F. Daniş, “Development of Interior Ballistic Simulation Software,” 2014.
- [13] M. a. Willcox, M. Q. Brewster, K. C. Tang, D. S. Stewart, and I. Kuznetsov, “Solid Rocket Motor Internal Ballistics Simulation Using Three-Dimensional Grain Burnback,” *J. Propuls. Power*, vol. 23, no. 3, pp. 575–584, 2007.
- [14] A. M. Tahsini, “SRM Performance Improvement: Erosive Burning Phenomenon,” in *Simulation*, 2006, no. July, pp. 1–5.
- [15] E. Cavallini, “Modeling and Numerical Simulation of Solid Rocket Motors Internal Ballistics,” Sapienza Universita Di Roma, 2009.
- [16] S. Nahon, “Nozzleless Solid Propellant Rocket Motors Experimental and Theoretical Investigations,” *AIAA/SAE/ASME 20th Jt. Propuls. Conf.*, 1984.
- [17] T. Liou and W. Lient, “Numerical Simulations of Injection-Driven Flows in a Two-Dimensional Nozzleless Solid-Rocket Motor,” *J. Propuls. Power*, vol. 11, no. 4, 1995.
- [18] S. Krishnan and K. K. Rajesh, “Erosive Burning of Ammonium Perchlorate/Hydroxyl-Terminated-Polybutadiene Propellants Under Supersonic Crossflows,” *J. Propuls. Power*, vol. 19, no. 4, pp. 623–631, 2003.
- [19] C. D. Mikkelsen and G. P. Roys, “Application of the Saderholm erosive burning model to nozzleless solid propellant rocket motors,” *J. Spacecr. Rockets*, vol. 21, no. 1, pp. 41–46, 1983.
- [20] H. S. Mukunda and P. J. Paul, “Universal behaviour in erosive burning of solid propellants,” *Combust. Flame*, vol. 109, no. 1–2, pp. 224–236, 1997.
- [21] A. Davenas, *Solid Rocket Propulsion Technology*. 1993.
- [22] C. Yıldırım, “Analysis of Grain Burnback and Internal Flow in Solid Propellant Rocket Motors in 3-Dimensins,” 2007.
- [23] J. C. Godon, J. Duterque, and G. Lengelle, “Solid-propellant erosive burning,” *J. Propuls. Power*, vol. 8, no. 4, pp. 741–747, 1992.
- [24] M. K. King, “Erosive Burning of Composite Solid Propellants: Experimental and Modeling Studies,” *J. Spacecr. Rockets*, vol. 16, no. 3, pp. 154–162, 1979.

- [25] R. Arora, X. Wu, F. X. White, and K. K. Kuo, “Erosive Burning of Composite Solid Propellants: Mechanism, Correlation, and Grain Design Applications,” *J. Spacecr. Rockets*, vol. 20, no. 1, pp. 43–48, 1983.
- [26] M. K. King, “Erosive burning of solid propellants,” vol. 9, no. 6, pp. 785–805, 1993.
- [27] E. M. Landsbaum, “Erosive Burning Revisited,” no. July, pp. 1–12, 2003.
- [28] L. R. Glick, “Temperature Sensitivity and Erosive Burning,” *J. Spacecr.*, vol. 16, no. 1, pp. 58–59, 1983.
- [29] C. Bornarke and Richard E. Sonntag, *Fundamentals of Thermodynamics*. 2008.
- [30] P. Colella and P. Woodward, “The piecewise parabolic method (PPM) for gas-dynamical simulations,” *J. Comput. Phys.*, vol. 54, no. 1, pp. 174–201, 1984.
- [31] M.-S. Liou, “Progress Towards an Improved CFD Method: AUSM+,” 1995.
- [32] A. Harten, “High Resolution Schemes for Hyperbolic Conservation Laws,” *J. Comput. Phys.*, vol. 135, no. 2, pp. 260–278, 1997.
- [33] H. C. Yee, “Linearized form of implicit TVD schemes for the multidimensional Euler and Navier-Stokes equations,” 1986.
- [34] E. Eraslan, “Implementation of Different Flux Evaluation Schemes Into a Two-Dimensional Euler Solver,” 2006.
- [35] P. . Roe, “Approximate Riemann solvers, parameter vectors, and difference schemes,” *J. Comput. Phys.*, vol. 43, no. 2, pp. 357–372, 1981.
- [36] Y. Wada and M.-S. Liou, “An Accurate and Robust Flux Spitting Scheme For Shock and Contact Discontinuities,” *SIAM J. Sci. Comput.*, vol. 18, no. 3, pp. 633–657, 1997.
- [37] J. L. Steger and R. F. Warming, “Flux Vector Splitting of the Inviscid Gasdynamic Equations with Application to Finite-Difference Methods,” *J. Comput. Phys.*, vol. 293, pp. 263–293, 1981.
- [38] B. Van Leer, “Flux-vector splitting for the Euler equations,” 1982.

- [39] R. H. Pletcher, J. C. Tannehill, and D. Anderson, "Computational Fluid Mechanics and Heat Transfer, Third Edition." p. 774, 1984.
- [40] M.-S. Liou and C. J. Steffen, "A new flux splitting scheme," *J. Comput. Phys.*, 1993.
- [41] J. Blazek, *Computational Fluid Dynamics: Principles and Applications*. 2001.
- [42] W. B. Lowrie, "Finite Element Solver for Flux-Source Equations," p. 147, 2008.
- [43] R. LeVeque, *Nonlinear conservation laws and finite volume methods for astrophysical fluid flow*, vol. M. 1998.
- [44] S. Gordon and B. J. McBride, "Computer Program for Calculation of Complex Chemical Equilibrium Compositions and Applications," no. October. 1994.